NTNU
Norwegian University of
Science and Technology

Application of the Linear Eddy Model

A Study of Differential Diffusion in Turbulent Hydrogen-Rich Jets

Nikolai Lid Bjørdalsbakke

Master of Science in Physics and Mathematics
Submission date: June 2018
Supervisor: Jon Andreas Støvneng, IFY
Co-supervisor: Sigurd Sannan, SINTEF Energi AS

Norwegian University of Science and Technology
Department of Physics

Abstract

Differential diffusion effects in turbulent reactive and non-reactive problems based on hydrogen-rich fuels are not yet fully investigated. Through use of a Fortran implementation of the Linear Eddy Model (LEM) realised in three dimensions as the LEM3D model, simulations were performed. The objective of this thesis is to investigate the differential diffusion in hydrogen-rich jets by application of the LEM3D code and ANSYS Fluent. Two configurations were used, a 90% H_2 and 10% Freon 22 ($CHClF_2$) jet issuing into air, as well as a 64% CO_2 and 36% H_2 jet placed in an air co-flow. The former configuration was performed for a Reynolds number $\mathrm{Re} = 20000$, while the LEM and Reynolds-averaged Navier–Stokes (RANS) resolutions were variable. The simulations were based on three different sets of Fluent input, named the coarse, fine and modified solutions according to their spatial resolutions. The second configuration was performed for a series of Reynolds numbers $\mathrm{Re} = 2000, 4000, 8000, 16000, 32000$, and 64000. The simulation results were used in order to investigate the accuracy of the Linear Eddy Model in 3D with respect to differential diffusion, and hence turbulent mixing of highly diffusive species such as hydrogen.

Compared to the experimental data for measurements done by Rayleigh scattering for the turbulent H_2/Freon 22 jet by Dibble et al. [1], the LEM3D displays reasonable agreement, but underestimates the data by almost an order of magnitude. The modified solution gave the LEM3D results which fit best with measurements. Raman scattering has been performed for a turbulent CO_2/H_2 jet by Smith et al. [2], and the LEM3D shows similar trends and value ranges to the experimental results, including decreasing effects of differential diffusion with higher values of Re. Large Eddy Simulation (LES) results produced by Maragkos et al. [3] only show vague agreement with LEM3D, and is overestimated by more than an order of magnitude.

Sammendrag

Effekter av differensiell diffusjon i turbulente reaktive og ikke-reaktive problemer basert på hydrogenrike brennstoffer er fremdeles ikke fullstendig utforskede. Ved bruk av en Fortran-implementasjon av den lineære virvelmodellen (LEM), realisert i tre dimensjoner som LEM3D, ble simuleringer utført. Målet med denne masteroppgaven er å undersøke differensiell diffusjon i turbulente, hydrogenrike stråler (heretter kalt jeter) ved anvendelse av LEM3D-kode og ANSYS Fluent. To forskjellige blandinger ble anvendt, en 90% H_2 og 10% Freon 22 ($CHClF_2$) jet inn i luft, i tillegg til en 64% CO_2 og 36% H_2 jet plassert i en langsgående luftstrømning. Førstnevnte konfigurasjon ble simulert for Reynoldstall $\mathrm{Re} = 20000$, der LEM og Reynolds-midlet Navier–Stokes (RANS) oppløsninger ble varierte. Simuleringene ble gjort på basis av tre ulike sett av Fluent-resultater, kalt den grove, fine og modifiserte løsningen i henhold til deres romlige oppløsning. Den andre jet-miksturen ble simulert for $\mathrm{Re} = 2000, 4000, 8000, 16000, 32000$, og 64000. Simuleringsresultatene ble bruk i den hensikt å undersøke nøyaktigheten til den lineære virvelmodellen i tre dimensjoner med hensyn på differensiell diffusjon og dermed turbulent miksing for svært diffusive stoffer som hydrogen.

Sammenliknet med eksperimentelle data for målinger utført ved hjelp av Rayleigh-spredning på den første jetkofigurasjonen av Dibble et al. [1], viser LEM3D noe overensstemmelse, men forutsier verdier som ligger nesten en størrelsesorden lavere. Den modifiserte løsningen gav LEM3D-resultatene med best overensstemmelse med målingene. Tilsvarende ble Raman-spredning utført for den andre strålekonfigurasjonen av Smith et al. [2], og LEM3D viser lignende trendlinjer og verdiområder, samt avtagende differensiell diffusjon med høyere Re-verdier. Resultater av store virvelsimuleringer (LES) fremstilt av Maragkos et al. [3] har kun vag overensstemmelse med LEM3D resultater, og blir overestimert med opptil flere størrelsesordener.

Preface

This work constitutes the Master's thesis of Nikolai Lid Bjørdalsbakke in technical physics with course code TFY4900. The focus of the thesis was proposed by SINTEF Energy Research, and I have been supervised by Dr. Sigurd Sannan at the Department of Thermal Energy, who has spent many enlightening meetings with me, offering constructive and valuable advice. Associate Prof. Jon Andreas Støvneng served as my formal co-supervisor, and provided assistance with problems and practical issues whenever I was in need of it.

The Master's thesis comprises 30 ECTS credits, and was my main focus throughout the semester it was written. Various tasks and problems have had to be handled to reach the final product which is represented by this thesis. The work has involved a literature review (see Appendix A), learning to work with different Linux based systems, computer clusters, ANSYS software, and parallel programming with MPI. The theoretical part of the work has revolved around understanding turbulence, the Linear Eddy Model in 3D, as well as analysing the LEM3D code developed by SINTEF. However, the main objective of the projects was to perform the actual simulations, which required understanding of turbulent properties, and experimental conditions. As a consequence, an investigation and understanding of the necessary input parameters also became important.

The personal motivation for the project is my interest in computational physics and fluid dynamics, and an interest in contributing to science connected to environmentally friendly energy solutions. The scientific motivation lies in the continued validation of the Linear Eddy Model, as well as the interest of calculating diffusive behaviour of hydrogen as a foundation for developing for example hydrogen combustion chambers.

The process of learning the theoretical subject matter while solving the problem, has proven to be an interesting way to work, but it has also caused me to end up in situations where solutions have been first found in hindsight. Experimenting with the code has given me insight, but it has also sometimes been a path of blind alleys and set-backs, so it might not always have been the most efficient way of approaching certain problems. However, as I have once previously worked with code and simulations on this scale in terms of both amount of lines of code and time scale, I was able to learn the workings of the code more efficiently than before. In the end I am pleased with the work I have done, and am proud to present it.

Finally, I would like to thank everyone who has supported me and shown an interest in the work I have been doing this spring. Again, I would like to thank my supervisors, Dr. Sannan and Assoc. Prof. Støvneng, for their steady guidance. I also owe many thanks to PhD candidate Fredrik Grøvdal who has given me a great deal of assistance, explained the theoretical foundation of the applied models to me, aided me in practical issues with simulations, and provided a framework for parallelising the LEM3D code.

This thesis concludes my 5 year long studies in Physics and Mathematics, effectively concluding a 19 year long education span. An effort I have found valuable, as it has provided me with new ways to see and interpret the world, and new ways of understanding nature. Still, I am eager to see what experiences, knowledge and challenges lie in wait for me, and look forward to the adventures which lie beyond this Master's thesis.

Table of Contents

List of Tables

List of Figures

Nomenclature

Greek Letters

α	Thermal diffusivity
α_{t}	Turbulent thermal diffusivity
δ_{edge}	The total width of the jet, defined as the lateral distance from the center axis to the point where the streamwise mean velocity component equals $0.01 \times U_{\mathrm{max}}$
$\delta_{i,j}$	Kronecker delta
$\delta(x)$	Jet width
Δt	Temporal discretization step length for a finite volume scheme
Δx	Spatial discretization step length for a finite volume scheme
ε	Turbulent energy dissipation
ζ	A rate parameter for triplet map events
η	Kolmogorov length scale
κ_{B}	Wave number of an eddy in the Batchelor length scale domain
λ	Bulk viscosity
Λ	Integral length scale
μ	Dynamic viscosity
μ_{t}	Turbulent dynamic viscosity
ν	Kinematic viscosity
ν_{t}	Turbulent kinematic viscosity, alternatively turbulent diffusivity
ξ	The mixture fraction

ρ	Mass density
$\tau_{i,j}$	The shear stress tensor for a fluid element
φ	An arbitrary scalar function

Latin Letters

3DCV	A cubic control volume in the LEM3D model constructed by three intersecting LEM domains
$\mathcal{ADV}_{3\mathrm{D}}$	An equation term accounting for advective motion
$c(x,t)$	General one dimensional scalar distribution
c	A constant scaling parameter
C	A general constant
C_μ	k-ε model parameter
$C_{1\varepsilon}$	k-ε model parameter
$C_{2\varepsilon}$	k-ε model parameter
$C(x,t)$	The result of a mapping from $c(x,t)$
datcst	LEM3D-code input parameter; The number of iterations before data collection starts
datmod	LEM3D-code input parameter; The number of iterations between each time statistics are collected for scalar profiles
d	LEM wafer thickness
D_j	Circular jet diameter
D_M	Molecular diffusivity
D_T	Turbulent diffusivity
E_B	Energy spectrum of Batchelor length scale eddies
f	A general Gaussian function
f_i	The i-component of an external force acting on a fluid element
f_C	Cumulative eddy center postition probability density function
$f(l)$	Linear Eddy Model probability density function for eddy lengths
F_i	The time averaged i component of an external force acting on a fluid element
h	An integer number of LEM wafers

i	The coordinate for the streamwise jet direction
isrc	LEM3D-code input parameter; A flag toggling the presence of heat sources in the flow
IMAX	The maximum number of 3DCVs in the x-dimension within the LEM3D-code
JMAX	The maximum number of 3DCVs in the y-dimension within the LEM3D-code
k	Turbulent kinetic energy
KMAX	The maximum number of 3DCVs in the z-dimension within the LEM3D-code
l	Length of an eddy, or a LEM triplet map event
L	A characteristic length scale for the flow
L_{mod}	A modified integral scale, scaled by a constant parameter
LEMres	LEM3D-code input parameter; LEM resolution, the number of LEM wafers per 3DCV edge length
LMXMAX	The maximum number of LEM wafers involved in a single triplet map eddy event
M	Resolution of LEM in 1D
M_x	The number of LEM wafers in a LEM1D domain in the x-direction
M_y	The number of LEM wafers in a LEM1D domain in the y-direction
M_z	The number of LEM wafers in a LEM1D domain in the z-direction
n	Number of threads running parallelised code
N	Frequency of triplet map events
N_x	The number of adjacent 1D LEM domains, or 3DCVs, in the x-direction
N_y	The number of adjacent 1D LEM domains, or 3DCVs, in the y-direction
N_z	The number of adjacent 1D LEM domains, or 3DCVs, in the z-direction
Ni	LEM3D-code input parameter; Number of 3DCVs in the x-direction
Nj	LEM3D-code input parameter; Number of 3DCVs in the y-direction
Nk	LEM3D-code input parameter; Number of 3DCVs in the z-direction
Nt	LEM3D-code input parameter; The number of iterations at the RANS advection time scale
p	Pressure

p'	The pressure fluctuation in a turbulent field
P	Average pressure
ProcNumber	The number of threads running an instance of the LEM3D code
r	Radial coordinate of a cylindrical symmetric function
RANSdx	LEM3D-code input parameter; The length of a cubic 3DCV edge
srcloc	LEM3D-code input parameter; The x-axis location of a thermal source
t	Time
t_0	An arbitrary point in time
t_1	An arbitrary point in time
T	A period of time for which the mean of a quantity in a turbulent field has negligible variations. Alternatively temperature
$\mathcal{T}$	An equation term governing turbulent motion
T_{DNS}	Total run time of a DNS simulation
T_{LEM3D}	Total run time of a LEM3D simulation
T_{t}	A turbulent time scale for the integral scale
u_i	The velocity i-component
u'	A characteristic velocity for the turbulent velocity fluctuations used in turbulent Reynolds numbers
u'_i	The i component velocity fluctuation in a turbulent field
u'_{rms}	Root-mean-squared turbulent velocity field fluctuation, also referred to as turbulence intensity
$\vec{U}$	The mean velocity field
U	A characteristic velocity for the flow scenario, used in Reynolds numbers
U_{coflow}	The air tunnel co-flow velocity at the same x-position as the jet inlet, i.e., where the air is entering the computational domain
U_{jet}	The velocity of the jet at the inlet
U_{max}	The maximum streamwise mean velocity component at a given position along the jet center axis
v	Velocity scale

varmod	LEM3D-code input parameter; The number of iterations between each time statistics is collected for scalar profiles along centerlines in j- and k-directions
velmod	LEM3D-code input parameter; The number of iterations between each time the average number of LEM wafers crossing 3DCV surfaces are computed
w	The ratio between two numbers of LEM wafers
x_i	The i-component of the spatial coordinate
x_0	An arbitrary position in the x-domain
Y	Mole fraction
z	The differential diffusion
z_{mean}	The mean differential diffusion
z_{rms}	The root-mean-squared differential diffusion

Acronyms

CFL	Courant-Friedrichs-Lewy number
DNS	Direct Numerical Simulation
LEM	The Linear Eddy Model
LEM3D	The Linear Eddy Model in 3D
LES	Large Eddy Simulation
RANS	Reynolds-averaged Navier–Stokes
RSM	Reynolds Stress Model

Fundamental parameters

Pr	Prandtl number
Pr_{t}	Turbulent Prandtl number
Re	Reynolds number
Re_{η}	Kolmogorov scale Reynolds number
Re_{t}	Turbulent Reynolds number
Sc	Schmidt number

Chapter 1

Introduction

Hydrogen is primed to be one of several important energy carriers over the coming years. Due to the pollution and environmental effects of carbon based fuels, the transition to more environmentally sensitive energy solutions will be necessary. Hydrogen gas is a suitable energy storage in this context as it produces H_2O as its single waste product during combustion or other energy exploiting processes. Hydrogen may even be extracted from for example methane (CH_4) which is a sustainable consumption of carbon fuels if it is combined with carbon capture and storage (CCS), since CO_2 is among the conversion process' waste products [4]. Hydrogen can also be extracted from biofuels and by electrolysis of water, making it available all over the world. And another advantage to traditional carbon-based fuels is that hydrogen has a far higher energy per mass content, up to three times. However, hydrogen does face challenges concerning storage when in its gas phase, because of the current lack of infrastructure supporting hydrogen. These factors and the currently high price of hydrogen production makes the risk far too high for any single company to try to introduce widespread societal consumption of hydrogen on as a single entity [5]. Despite this, Demirbas predicts that hydrogen based energy consumption will satisfy 34 % of global energy demand by 2050 also considering the estimate that the global petroleum reserves are said to be depleted in 50 years [6]. Hydrogen faces competition from the pure consumption of bio-fuels and from battery technology, but Ball et al. claim that the major use of hydrogen will be in automotive transport through fuel cell technology, and that with the current state of the competitors, hydrogen has some advantages that may push it ahead in this competition [5].

As Ball et al. underlines, policy support and larger initiatives from multiple stakeholders are necessary to make a hydrogen society come to fruition. In Europe, research initiatives such as the Fuel Cell and Hydrogen Joint Undertaking (HFC JU), supported by the European Union's Horizon 2020 programme will research, develop and demonstrate hydrogen technologies that may prove to be sustainable [7]. As mentioned, the assumed to be most widely utilised means of extraction energy from hydrogen is fuel cells, however hydrogen may also have applications within combustion in for example gas turbines. The mixture of hydrogen and air is a highly combustible mixture which also carries a certain risk. In for example nuclear reactors, the formation of hydrogen gas may lead to hazardous situations as has been put in the spotlight since the Fukushima accident of 2011. Satiah et al. stress that computational tools are essential in such a context [8].

Enter the Linear Eddy Model (LEM), a model for turbulent molecular mixing which works differently to other turbulence models in that it is not solving any equations directly but instead rearranges scalar fields and introduces gradients. It was conceived and developed by A. Kerstein in the late 1980s and is inherently a one-dimensional model [9, 10]. SINTEF Energy has built upon the LEM and developed a three-dimensional model known as the LEM3D [11]. Many competing computational approaches may be applied to hydrogen flows such as direct numerical simulations (DNS) [12], Reynolds-averaged Navier–Stokes (RANS) [13] or Large Eddy Simulations (LES) [3]. Even the standalone LEM has been applied to diffusion in hydrogen-rich jets, as demonstrated by Dibble et al. [1]. The LEM is a computationally efficient model and saves a lot of computational time compared to other methods. Weydahl has compared the run time of a DNS simulation to an equivalent LEM3D simulation and expressed the result as follows,

$$T_{\mathrm{LEM3D}} = \frac{T_{\mathrm{DNS}}}{M^2}, \tag{1.1}$$

where T_{LEM3D} and T_{DNS} are the total computational time for the LEM3D and DNS simulations, while M is the one-dimensional resolution of the LEM [14]. This proves the LEM3D to be a low cost model. Even though the model is economical, it is originally written in sequential code, and any code which can be parallelised may benefit from it. Parallel programming is a useful technique, which drastically reduces run times whenever it is run on systems with a large number of CPUs, or CPU cores. Even simply four or six cores may give a noticeable reduction in run time. Hence, spending time parallelising sequential code will most likely pay off, since run time is reduced which further will lessen the consequences whenever a simulation is initiated with the wrong parameters or if it goes awry somehow else.

Due to the potential in hydrogen as an energy carrier, SINTEF has allotted many resources and projects to hydrogen research, and as such application of the LEM3D to hydrogen-rich flows is only natural. Hydrogen, which is the lightest element has diffusive properties different to heavier elements and compounds. Traditionally in mixed flows, different species have been assumed to have the same diffusivity [15]. This is therefore a poor assumption for flows containing hydrogen species. That is why measuring differential diffusion and its effect on molecular mixing is advantageous, and may uncover important implications for combustion properties [16]. It is known that the effects of differential diffusion decreases with higher Reynolds numbers, but the decrease has proven to be slower than initially assumed. Capturing this effect is then an important feature for the validation of any turbulence model.

The aim of the work presented in this paper is to investigate turbulent, hydrogen-rich jets propagating into air. Different hydrogen mixtures will be considered, and computational results will be compared to other computational and experimental results. This will give grounds for assessing the performance and precision of the LEM3D, and may yield some more insight into differential diffusion, since the LEM is a model is a mechanistically correct model. This work is to a large extent based on the work done by Sannan and Kerstein, and aims to build upon and add detail to the results [16, 17].

Chapter 2

Theory

2.1 Governing Equations

The most general equations describing momentum conservation in constant density fluid flows are the Navier–Stokes equations

$$\frac{\partial u_i}{\partial t} + u_j \frac{\partial u_i}{\partial x_j} = \frac{1}{\rho} \frac{\partial \tau_{i,j}}{\partial x_j} + f_i, \tag{2.1}$$

where u_i is the i-th velocity component, f_i is the i-component of an external force, $\tau_{i,j}$ is the shear stress tensor, and ρ is the fluid mass density [18, p. 68]. The equation has no known analytical solutions, but may be solved numerically. For the present work only subsonic, incompressible flows at constant pressure are treated. All (chemical and nuclear) reactions are neglected and so are their source terms, since the examined flows are non-reactive. The above equation accounts for conservation of momentum, and mass conservation is expressed by the continuity equation

$$\frac{\partial u_j}{\partial x_j} = 0, \tag{2.2}$$

which is given under the continued assumption of incompressible flow. Diffusive and advective transport of a scalar field φ is in this work described by the equation

$$\frac{\partial \varphi}{\partial t} = \frac{\partial}{\partial x_j}\left(D_{\mathrm{M}} \frac{\partial \varphi}{\partial x_j} \right) + \mathcal{T} + \mathcal{ADV}_{\mathrm{3D}}, \tag{2.3}$$

where D_{M} is the molecular diffusivity. $\mathcal{T}$ is the term incorporating turbulent transport, as for example governed by scalar field rearrangements which will be described in context of the LEM in a coming subsection. The term $\mathcal{ADV}_{\mathrm{3D}}$ is a term accounting for Lagrangian advective transport processes, and coupling of control volumes and intersecting domains [11]. The advection is governed by the mean velocity flow field, $\vec{U}$, which may be supplied externally from a flow solver.

2.2 Diffusion

Diffusion is the natural process where a gradient in some physical property induces movement in the property or particle such that the gradient is lessened in magnitude. Hence, nature counteracts gradients in materials. The first term on the right hand side of Equation (2.1) expresses viscous diffusion, and the same term in Equation (2.3) is handling molecular diffusion. The Schmidt number relates these two fluid properties in a parameter

$$\mathrm{Sc} = \frac{\nu}{\mathrm{D_M}}, \tag{2.4}$$

which is an important parameter when looking at the diffusive behaviour of a flow problem. ν is the kinematic viscosity. Another fundamental diffusion parameter is the Prandtl number which is the dimensionless ratio between momentum induced diffusivity (or viscosity), and the thermal diffusivity α. The parameter assumes the form in laminar and turbulent flow respectively as

$$\mathrm{Pr} = \frac{\nu}{\alpha}, \text{ and } \mathrm{Pr_t} = \frac{\nu_\mathrm{t}}{\alpha_\mathrm{t}}. \tag{2.5}$$

2.2.1 Differential Diffusion

Differential diffusion is a measure introduced to determine the mixing of species due to differing diffusive properties. The mixture fraction of a species l is defined as

$$\xi_l = \frac{Y_l - Y_{l,2}}{Y_{l,1} - Y_{l,2}}, \tag{2.6}$$

where Y_l is the mole fraction in the mixture, and $Y_{l,s}$ is the mole fraction of species l in incoming stream s. By subtracting the mixture fractions of two species l and m, where $l \neq m$, the differential diffusion is defined as

$$z = \xi_l - \xi_m. \tag{2.7}$$

2.3 Turbulence

For a fluid flow, a dimensionless number known as the Reynolds number can be defined. The number is defined as

$$\mathrm{Re} = \frac{\rho U L}{\mu}, \tag{2.8}$$

for a fluid with dynamic viscosity $\mu = \nu\rho$. U is a velocity scale for the flow field, while L is a characteristic length scale for the fluid in question. For sufficiently high Reynolds numbers, laminar flow and motion transition into turbulence. Turbulent flow is characteristically different from laminar flow in that it is fluctuating and disorderly fluid motion. White summarises turbulence in this way in his book on viscous fluid flows [18, p.400]:

> *“A spatially varying mean flow with superimposed three-dimensional random fluctuations that are self-sustaining and enhance mixing, diffusion, entrainment and dissipation.”*

Fluctuations appear in the pressure, the temperature, and the velocity in all the dimensional directions. The fluctuations can be regarded as superimposed around the mean value of the properties. For a turbulent flow with velocity components u_i and pressure p they can be expressed as

$$\begin{aligned} u_i &= U_i + u_i', \\ p &= P + p', \end{aligned} \tag{2.9}$$

where p' and u_i' are the fluctuations around the means U_i and P. The mean is here defined as the time averaged value;

$$\Phi = \bar{\varphi} = \frac{1}{T} \int_{t_0}^{t_0+T} \varphi(t) dt, \tag{2.10}$$

where φ is a general time dependent quantity. The time T is larger than the time scale for the fluctuations, but shorter than the time scale for variations in the mean value. As a measure for the magnitude of velocity fluctuations, the turbulence intensity, or root-mean-squared velocity fluctuation u'_{rms}, can be used. It is defined as

$$u'_{\mathrm{rms}} = \sqrt{\frac{1}{T} \int_{t_0}^{t_0+T} {u_i'}^2 dt}. \tag{2.11}$$

Introducing a measure of the energy carried by the turbulent part of the flow, the turbulent kinetic energy may be defined as,

$$k = \frac{1}{2} u_i' u_i', \tag{2.12}$$

where Einstein’s summation convention is applied. A turbulent flow contains eddies, which are packets of fluid often moving in a swirling motion. Eddies both appear and disintegrate into smaller eddies over a large spectrum of time scales. The eddies are often categorised by three length scales; the integral scale, the intermediate (or often known as the Taylor) scale, and the Kolmogorov scale. According to Kolmogorov’s theory, the largest eddies belonging to the integral length scale, Λ, transfer their energy to smaller eddies when they break down, and thus the energy cascades down until eddies on the Kolmogorov length scale, η, and below are reached. The integral scale process is illustrated in Figure 2.1. A turbulent Reynolds number can be determined for the integral scale as

$$\mathrm{Re_t} = \frac{u' \Lambda}{\nu}. \tag{2.13}$$

Similarly the Reynolds number for the Kolmogorov scale eddies may be given as:

$$\mathrm{Re}_\eta = \frac{v \eta}{\nu} = 1. \tag{2.14}$$

Here, v is a velocity scale defined such that Re_η is equal to 1, which it is by definition [19, p.130,137]. The largest eddies carry most of the energy in the turbulent flow while the

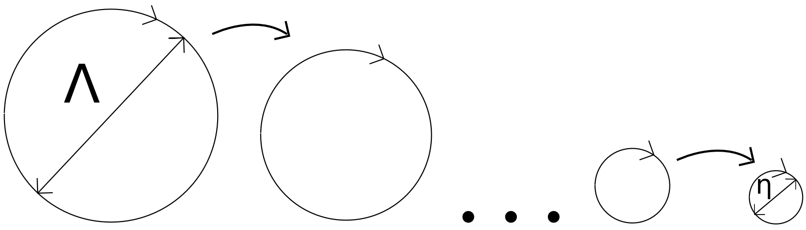

Figure 2.1: A simple illustration of the Kolmogorov cascade. Larger eddies, starting at the integral scale, Λ, breaks down into more and gradually smaller eddies, transferring energy into the new eddies until the Kolmogorov length scale, η, is reached.

Kolmogorov scale eddies feel the viscous effects of the fluid and dissipates energy carried by the flow. Kolmogorov hypothesises that smaller scale eddies are independent of the larger eddies and the mean flow, and that they are isotropic, which means that all directions are equally probable for the eddies to move in [19, p.127]. The Kolmogorov scale eddies represent the smallest eddies, in which kinetic energy is dissipated by viscous diffusion processes. The smallest eddies do not contribute much to overall transport in terms of distance, but are broken down on the molecular level and greatly enhances molecular mixing compared to ordinary laminar flow [19, p.124]. A relationship between the integral and Kolmogorov scales is derived by Weydahl [14], and appears as

$$\frac{\eta}{\Lambda} \sim Re_{\mathrm{t}}^{-\frac{3}{4}}. \tag{2.15}$$

The fluid particles transported by many turbulent eddies perform a random walk, and the transport by this motion may be classified as the turbulent diffusivity D_{T}, with units m^2/s. By dimensional analysis and the turbulent time scale, T_{t}, the relations

$$D_{\mathrm{T}} \sim \frac{\Lambda^2}{T_{\mathrm{t}}}, \; T_{\mathrm{t}} \sim \frac{\Lambda}{u'},$$

are uncovered. Further, using the relation (2.15) it can then be derived that the turbulent diffusivity scales as

$$D_{\mathrm{T}} \sim u'\Lambda = \nu \mathrm{Re}_{\mathrm{t}} \sim \left(\frac{\Lambda}{\eta}\right)^{\frac{4}{3}}.$$

Finally, based on this the scaling with eddy size l is assumed to be [20]

$$D_{\mathrm{T}}(l) \sim l^{\frac{4}{3}}. \tag{2.16}$$

2.3.1 RANS

The Navier–Stokes equations (2.1) may be solved numerically, but this process is computationally very demanding by current hardware standards. Removing some information by averaging the equation, makes it more computationally affordable for turbulent flows, but then results in identifying the mean velocity field. For Newtonian fluids, the stress tensor is

$$\tau_{i,j} = -p\delta_{i,j} + \mu\left(\frac{\partial u_i}{\partial x_j} + \frac{\partial u_j}{\partial x_i}\right) + \lambda\delta_{i,j}\frac{\partial u_k}{\partial x_k}. \tag{2.17}$$

Here, μ is the dynamic viscosity, λ is the bulk viscosity, and $\delta_{i,j}$ is the Kronecker delta. By inserting this into Equation (2.1), and introducing the decomposition for velocity and pressure in the equations (2.9), and then averaging the equation as per Equation (2.10), the Reynolds-averaged Navier–Stokes (RANS) equations may be obtained,

$$\frac{\partial U_i}{\partial t} + U_j\frac{\partial U_i}{\partial x_j} = -\frac{1}{\rho}\frac{\partial}{\partial x_j}\left(P\delta_{i,j} + \rho\overline{u_i'u_j'}\right) + \nu\frac{\partial^2 U_i}{\partial x_j^2} + F_i. \tag{2.18}$$

Here, F_i is the time averaged i-component of the external force. The $\rho\overline{u_i'u_j'}$ are the turbulent stress components, and must be modelled by a turbulence model. A common model is the k-ε model which sets up and solves transport equations for the turbulent kinetic energy k, and the dissipation of turbulent energy ε.

In the RANS framework, the turbulent viscosity can be defined as

$$\mu_\mathrm{t} = C_\mu\rho\frac{k^2}{\varepsilon}, \tag{2.19}$$

where $C_\mu = 0.09$. From Prandtl's mixing length model, the relation between the integral scale and the turbulent dissipation can be constructed by dimensional analysis arguments [19, p. 52, 138], and takes the form

$$\Lambda = C_\mu^{\frac{3}{4}}\frac{k^{\frac{3}{2}}}{\varepsilon}. \tag{2.20}$$

2.4 Jets

The definition of a jet in the context of this thesis is a fluid or mixture flow entering a still fluid consisting of different species, through a circular nozzle. The flow is considered to have a sufficiently high Reynolds number to be turbulent, and for the remainder of the thesis the term "jet" means an axisymmetric turbulent jet.

A turbulent jet, see Figure 2.2, consists of a potential core, mixing layers where the surrounding fluid is entrained into the incoming jet, and the self-similar region which is established an integer multiple of inlet diameters downstream. The self-similar region is defined as the part of the jet where a Gaussian mean velocity profile has developed for which

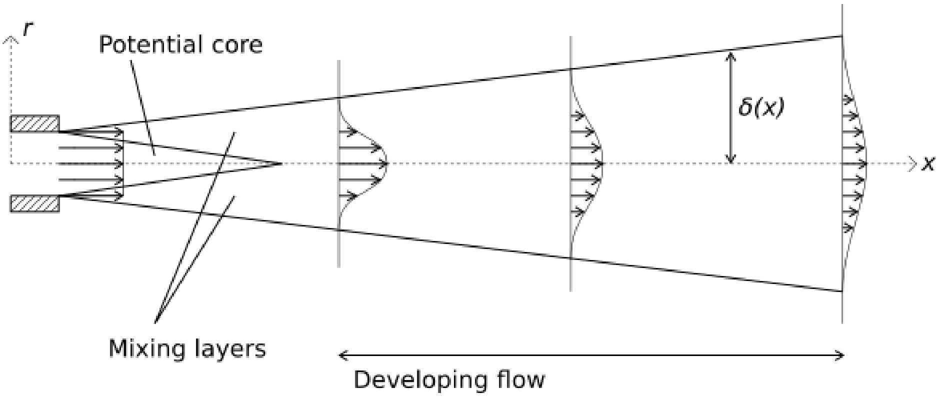

Figure 2.2: An illustration of the streamwise mean velocity (U_i) profile development for an axisymmetric turbulent jet. The general internal structure near the inlet is illustrated, as well as the jet width $\delta(x)$. The jet center axis coincides with the x-axis.

$$\frac{U_i}{U_{\max}} = f\left(\frac{r}{\delta}\right), \tag{2.21}$$

where f is a Gaussian function, and $U_{\max}$ is the maximum velocity of the velocity profile at the given downstream location. A jet expands in cross section as the distance from the inlet increases, and the width of the jet δ varies as a linear function of x, i.e., $\delta(x) \sim Cx$, where C is a constant.

For the simulations performed in this thesis the circular inlet is approximated by a square inlet in order to apply a Cartesian mesh consisting of perfect cubic control volumes (3DCVs). Kim et al. [21] have by means of numerical simulation in ANSYS Fluent using RANS with Reynolds Stress Modelling (RSM) examined differences in downstream development of turbulent jets with different inlet geometries. Square inlets have then been shown to have a slightly wider mean velocity distribution, i.e. more spreading, in the self-similar region downstream, compared to a circular inlet. The square jet no longer has an axisymmetric flow, but mixing is enhanced.

2.5 The Linear Eddy Model

The Linear Eddy Model is a model representing turbulent eddies and mixing of scalars in a one-dimensional domain. It is a technique based on stochastic rearrangement events of the species' position, in contrast to other computational approaches such as Direct Numerical Simulation which solves the governing equations directly. The drawback of DNS is that for sufficient resolution to resolve the smallest scale eddies, it demands an extreme amount of computational power and time. The aim of the Linear Eddy Model is to greatly reduce this computational time without sacrificing resolution and while still treating turbulent advection as an advective process. LEM is not only a tool for making predictions in turbulent flow, it also gives a mechanistically correct picture of turbulent flow, and can be used to study the physics of such problems unlike other computational models based on the gradient diffusion hypothesis [20]. Being a model for molecular mixing, the LEM lends itself well to reacting flows and combustion problems, however this will not be the focus of the following since the present work treats non-reacting flows.

2.5.1 LEM in 1D

The LEM can resolve the full range of turbulent length scales from the integral scale down to the Kolmogorov scale, as well as all turbulent time scales [20], while being less computationally demanding than for instance DNS. The model has been combined with other turbulence simulation techniques in the past. LEM can be used as a subgrid model for methods such as Large Scale Eddy Simulations (LES) which simulates the mean flow and larger eddies. LEM is then used for modelling of the smallest eddies. In the present subsection, LEM will be presented in its standalone 1D form.

The Triplet Map

Equation (2.3) describes transport of a scalar field φ. It can easily be modified to handle even turbulent reactive flow, by adding a term to represent reactions. LEM handles the convection term $\mathcal{T}$ in a characteristic way, which us by executing stochastically occurring stirring events in the one-dimensional domain. The events are modelled, both temporally and spatially, by randomly selecting the location and length of the stirring rearrangement for each event. This is done though a permutation, the triplet map. The length is determined based upon the values for the turbulent length scales set for the given case. The LEM triplet map is a mapping from $c(x,t)$ to $C(x,t)$, applied to a segment of length l, $[x_0, x_0+l]$ at the time t. The mapping is defined as follows:

$$C(x,t) = \begin{cases} c(3x-2x_0,t), & \text{for } x_0 \le x \le x_0 + \frac{1}{3}l, \\ c(-3x+4x_0+2l,t) & \text{for } x_0 + \frac{1}{3}l \le x \le x_0 + \frac{2}{3}l, \\ c(3x-2x_0-2l,t) & \text{for } x_0 + \frac{2}{3}l \le x \le x_0 + l, \\ c(x,t) & \text{otherwise.} \end{cases} \tag{2.22}$$

In this way the scalar species concentration profile is rearranged. An example for a linear concentration gradient is shown in Figure 2.3. This rearrangement mimics the way the scalars are transported convectively for the swirling motion of an eddy in 3D, such that the 1D triplet map intersects this mixing motion. Hence, the LEM mechanistically resembles turbulent transport. The eddy motion induces enhanced gradients, as can be seen from the triplet mapping formulation. A drawback of the model is that it introduces discontinuities in $\frac{\partial C}{\partial x}$, as is evident from Figure 2.3. This leads to faster than expected fall-off for high-wavenumber eddies in the Batchelor energy spectrum $\kappa_B^2 E_B(\kappa_B)$. κ_B, is a wave number on the Batchelor length scale, which is the scale at which molecular-diffusive smoothing can counteract strained wrinkling of the scalar field. Hence, there are fewer eddies of short length scales than expected [10].

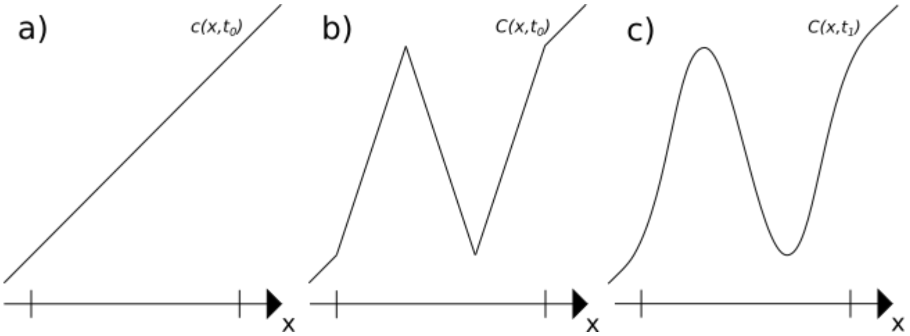

Figure 2.3: A linear one-dimensional scalar field is; a) in its initial state, b) subjected to an instantaneous triplet map stirring event, c) experiencing diffusive effects as the solution of the diffusion equation has been propagated in time to t_1.

The Rate of Events

If one considers a particle transported by turbulent motion in the x-dimension, its turbulent diffusivity can be expressed as

$$D_{\mathrm{T}} = \frac{1}{2} N \langle x^2 \rangle, \tag{2.23}$$

where $N = \zeta l$ is the frequency of events, ζ is a rate parameter, and l is the length of the stirring event [20]. It can be shown that for a particle in a stirring event the mean square displacement $\langle x^2 \rangle$ takes the form such that,

$$D_{\mathrm{T}} = \frac{2}{27} \zeta l^3. \tag{2.24}$$

Generalising this to be valid for a wider range of eddy lengths around l, the diffusivity is [22]

$$D_{\mathrm{T}} = \frac{2}{27} \zeta l^3 f(l) dl. \tag{2.25}$$

In a fluid flow the fraction of the eddies which has lengths in the range $[l, l + dl]$ are expressed as $f(l)dl$, where $f(l)$ is the probability density function satisfying

$$\int_{\eta}^{\Lambda} f(l) dl = 1. \tag{2.26}$$

Making use of the normalisation, Equation (2.25) and the assumption that the turbulent diffusivity is proportional to $l^{\frac{4}{3}}$ from Equation (2.16), the function $f(l)$ can be shown, see [22], to have the form

$$f(l) = \frac{5}{3} \frac{l^{-8/3}}{\eta^{-5/3} - \Lambda^{-5/3}}. \tag{2.27}$$

By finding the expectation value of D_{T} by integration over l for Equation (2.25), and using the relation (2.16) showing that $D_{\mathrm{T}} \sim \nu \mathrm{Re}_{\mathrm{t}}$ this leads to an expression for the number of events given as [22];

$$N = \zeta l = \frac{54}{5} \frac{\nu \, \mathrm{Re}_{\mathrm{t}}}{\Lambda^3} \frac{(\Lambda/\eta)^{5/3} - 1}{1 - (\eta/\Lambda)^{4/3}} l. \tag{2.28}$$

In essence, the triplet map rearrangements are statistically independent events that occur instantaneously, similar to a Poisson process. In contrast, the diffusion solving is steadily advanced in time as stirring events occur randomly throughout the simulation according to the event frequency ζ. Hence, an important assumption in LEM is that turbulent eddies are statistically independent events. This also emphasises how LEM makes a clear distinction in its treatment of convective (turbulent) and diffusive species transport [10, 20]. The equations (2.27) and (2.28) are the foundations for how triplet maps are implemented in code.

2.5.2 LEM3D

The model presented in the current subsection is based on the model presented by Sannan et al. in 2013 [11]. In contrast to CFD, the LEM3D treats advection and mixing of fluid cells as opposed to solving flow field equations. LEM3D is in some ways a straight forward development of the 1D LEM, in the sense that it is constructed as a mesh of 3DCVs containing intersecting and independent 1D LEM domains in all three dimensions. The independent domains makes the model suitable for parallel execution. Three arrays of $N_x \times N_y$, $N_x \times N_z$ and $N_y \times N_z$ LEM domains, each domain containing M_z, M_y or M_x 2D LEM-wafers for each array respectively. The intersection between three 1D LEM domains, one from each array, constitutes and bounds a 3DCV. See Figure 2.4 for an illustration of the model's geometrical composition. In terms of resolution, the parameter LEMres is used here, and is the number of LEM-wafers $M_{x/y/z}$ divided by number of 3DCVs within that particular domain. The intersecting, yet independent LEM domains do introduce a few problems not encountered in the 1D version which must be addressed, such as three simultaneous co-located representations of the same volume, and limited mixing between adjacent 1D domains. Also, LEM3D requires flow field input from either a CFD framework, analytic expressions or experimental data, and is therefore not a complete flow solver on its own, only a mixing framework.

LEM3D makes use of several assumptions. First of all it considers incompressible flow, which means decoupling the pressure and velocity fields. Thermal expansion and density changes is included when reacting flows are considered. The version of the model considered in this thesis assumes a constant mean flow field, i.e. a steady state solution, which also means neglecting effects from counter gradients induced by triplet map stirring which would otherwise affect the mean flow field. This assumption can be discarded if backward coupling to a flow solver, or data, is a part of the model solution setup.

Since molecular mixing and turbulent stirring is resolved down to Kolmogorov scale,

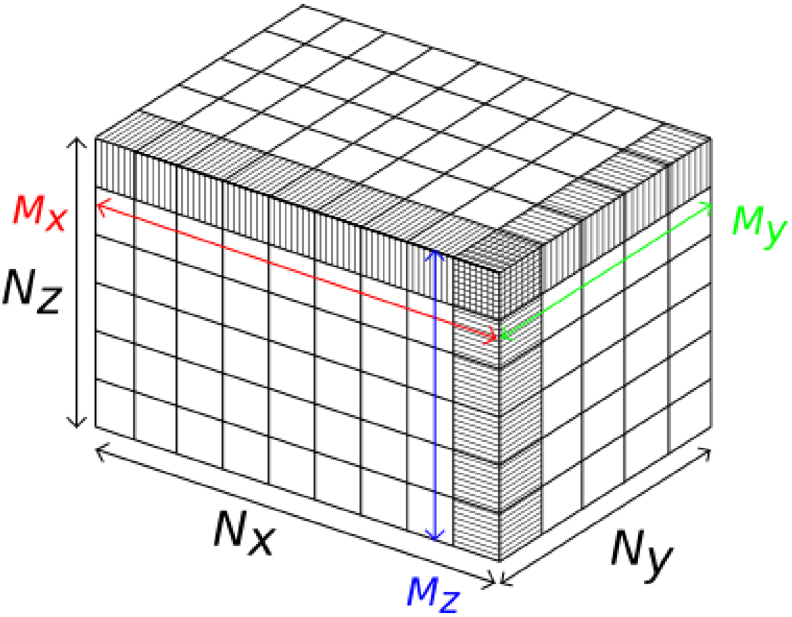

Figure 2.4: The three array mesh constructed by $N_x \times N_y \times N_z$ control volumes. Three 1D LEM domains are shown to intersect and create a cubic 3DCV, each domain consisting of either M_x, M_y or M_z LEM wafers according to axial direction.

the LEM-wafers are similar to a perfectly stirred reactors (PSR) [14]. This means that mixing is resolved at all scales and all wafers are homogeneous perfect mixtures where also substances entering the wafer are instantly perfectly mixed. A PSR is a reactor that is well macro- and micromixed. A well macromixed mixture has a uniform distribution making scalar fields independent of the spatial coordinates mapping the mixture, while a well micromixed mixture has zero scalar variance, and LEM-processes take care of both scales of mixing. If a resolution cut-off is set at a higher scale than the Kolmogorov scale, then all scales not resolved are assumed to also be perfectly stirred mixtures.

Another major assumption incorporated in the model is that turbulence at all scales is isotropic, and in nature this is only a fact at small turbulent scales. In addition, turbulent eddies are assumed to only appear in the planes parallel to the three main axes, no eddies tilted with regards to these axes appear. The eddies restricted to the planes are also different to real eddies since the 3D structure of an eddy may be more cylindrical, it may be curved, and may even transport other smaller eddies as if the smaller eddies were frozen in time. In comparison, the eddies modelled in LEM3D are simplified. The 1D triplet maps are based on lines of sight through a 3D eddy, but may be represented for visualisation as a perfect circular cross section from a 3D eddy. Figure 2.5 contrasts the two eddy types. Similar to triplet maps, molecular diffusion is only allowed in the direction of the 1D LEM domains, i.e. along the coordinate axes, even though diffusion in reality may happen in all spatial directions.

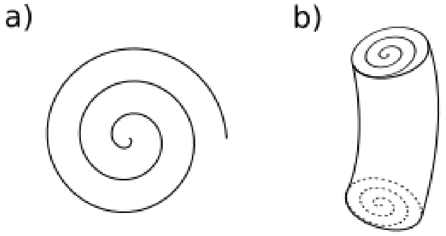

Figure 2.5: A comparison of idealised eddies, and an example of a more realistic 3D eddy. In part a) a circular 3D eddy cross section is illustrated as a simple swirl, while in b) a curved cylindrical quasi-3D eddy is presented.

Equation (2.3) has a term describing advective transport, including domain coupling. In LEM3D, Lagrangian treatment of advection is applied. This means the LEM wafers are simply displaced according to the velocity field, as opposed to using Eulerian finite differences [14]. However, the three arrays of LEM domains are all simultaneous individual representations of the computational domain, and therefore all extensive properties such as scalar concentration fields are tripled. As a consequence, the transport through the boundaries of each 3DCV is set three times as large as for a single representation of the computational domain. The solution reached in LEM3D is simply to multiply velocities by three, which may be unsuitable concerning the effect on Reynolds numbers, but has for previous work performed decently [11].

For each LEM domain all advective transport only happens in one direction. This introduces yet another problem with the model composition, since this hinders substances mixing with neighbouring domains. To remedy this, random 90° rotations around a a randomly chosen axis of the 3DCVs were introduced. The rotation frequency is set using the time the flow field would use to transport a particle through the 3DCV in question. The rotations do also mimic turbulent eddies in some sense, but the solution also has a drawback in that sharp, unphysical gradients are introduced. Figure 2.6 illustrates the effects of the rotations for a 2D case.

The probability density function for eddy lengths in triplet maps has been reformulated for use in LEM3D and is presented by Sannan et al. [11] in this form:

$$f(\hat{h}) = \frac{\hat{h}^{-\frac{8}{3}}}{\sum_{h=h_{\mathrm{min}}}^{h_{\mathrm{max}}} h^{-\frac{8}{3}}}. \tag{2.29}$$

Here, h is an integer number of LEM cells. h_{min} and h_{max} is determined by an approximate integral scale $L_{\mathrm{mod}} = 3h_{\mathrm{max}}d$, related to the measured integral scale Λ by an adjustable parameter c, such that $L_{\mathrm{mod}} = c\Lambda$. The parameter c can be adjusted for best fits to scalar mixing properties [11], and to the scalar fields passed to LEM3D from external sources. h_{min} is determined exactly analogously for the Kolmogorov scale η, while d is the LEM wafer thickness. The rate of events is rewritten in the following form

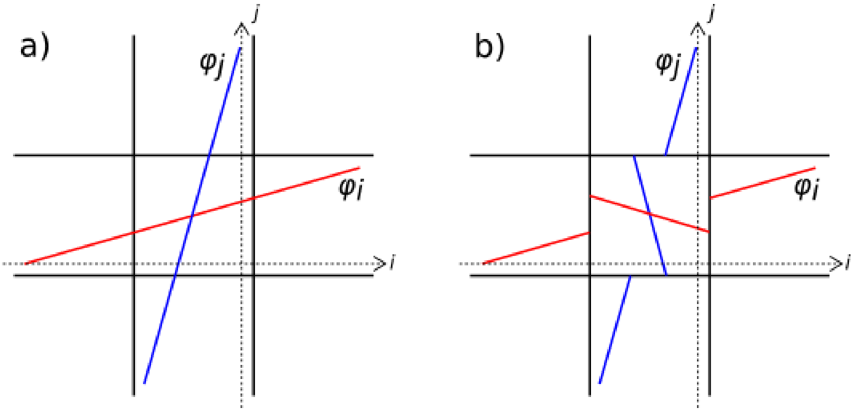

Figure 2.6: Part a) shows the intersection of two 1D LEM domains in directions i and j, with the profiles of a scalar values φ_i and φ_j for each domain respectively. The domain intersection is rotated 90° clockwise, such that the intersection segments are effectively interchanged between the domains. The resulting scalar profiles are shown in part b).

$$\zeta = \frac{D_\mathrm{T}}{2d^3}\left(\sum_{h=h_\mathrm{min}}^{h_\mathrm{max}} h^2(h-1)f(h)\right)^{-1}, \tag{2.30}$$

for ease of implementation. Finally, selecting positions of the triplet maps are implemented by creating a probability density function for the 3DCVs using the rate of events for each cell. The cumulative eddy center position probability density function is implemented in the following way for an arbitrary direction s,

$$f_C(N_s) = f_C(N_s - 1) + \frac{\zeta(N_s)}{\sum_{N_s}\zeta(N_s)}. \tag{2.31}$$

Here, N_s is the position of a 3DCV in direction s. It is initialised by $f_C(1) = \zeta(1)/\sum_{N_s}\zeta(N_s)$. The three equations (2.29), (2.30) and (2.31) determine all properties of triplet map eddies, in practice.

LEM3D is not yet a complete model because some of the problems highlighted above are yet to be solved, such as the lateral mixing of species, and triple simultaneous representations of domains. As demonstrated, solutions have been proposed and implemented, but they often introduce other problems. It is likely that these additional problems may be corrected by continued refinement of the model, or by alternative solutions. For example, methods of transporting wafers laterally between domains can possibly be linked to turbulent behaviour without rotating domains, or some additional coupling may be done after rotations. Further validation of the model is needed before it is known whether the model will give a realistic and quantitatively more precise solution to turbulent mixing problems, and can compete with DNS and other quantitative computational approaches.

Chapter 3

Computational Method

3.1 Software and Code

This section concerns itself mainly with the type of software used, and the implementation of the LEM3D code.

3.1.1 Various Tools

For the current work, a variety of different software was used for various tasks, among these is the ANSYS software package, including the subprograms Fluent, DesignModeler, and Meshing. The other software used was MatLab, Maple, and InkScape. See Table 3.1 for details on what versions were used.

MatLab, was used for different tasks, but mainly to treat coordinate setups, plots and post-processing of the results whenever needed. GNUplot was used for viewing simple plots consecutively as the results were finished. For the creation of illustrative figures for this paper, InkScape was employed. Maple was used for processing input data and computing some necessary parameters. The use of ANSYS will be explained in detail in Subsection 3.2.1.

3.1.2 LEM3D

The LEM3D is implemented Fortran 77/90 in a straightforward, linear fashion. The starting point is to initialise, load, and test the validity of data, and whether the simulation is new or to be restarted. The main loop iterating over the RANS scale time steps is then started. Within this loop all LEM domains and 3D control volumes are visited. First, the advection routine is implemented according to the LEM3D model description, before the 3DCVs are rotated. Then the LEM processes are initiated. At the end of a set interval of loop iterations, data is collected and restart files may be written. After the loop has

Name	Version(s)
ANSYS	18.1, 17.2
MatLab	2014b
Maple	2017
Inkscape	0.91
Gnuplot	5.0

Table 3.1: The programs used to create, analyse and present data, as well as prepare input for the LEM3D code.

finished its iterations, the data is post processed and written to file. See Figure 3.1 for an illustration of the code structure.

The most central parts of the program are the subroutines handling the LEM domains and their triplet map rearrangements, as well as the 3DCV rotation and advection routines. In the main loop, the LEM domain routines are executed every single iteration and are responsible both for triplet maps and molecular diffusive processes. Several iterations are performed in order to resolve shorter time scales than the RANS advection time steps, which makes this part of the code very computationally intensive. The diffusion equation is solved during the time intervals between each triplet map event. It is solved by the implicit Euler scheme in time, and by central difference in space, giving the discretised equation

$$-C\varphi_{j-1}^{n+1} + (1+2C)\varphi_j^{n+1} - C\varphi_{j+1}^{n+1} = \varphi_j^n.$$

This finite difference scheme then gives the diffusive development of the scalar value φ of wafer $\#j$ in a 1D LEM domain from time step n to $n+1$. C is the CFL-number defined as $\frac{D_\mathrm{M}\Delta t}{\Delta x^2}$, where Δx and Δt are the discretisation steps in space and time, while D_M is the molecular diffusivity. This can be arranged as a tridiagional matrix system for the entire domain. For the current code Neumann boundary conditions are used at the domain boundaries such that there are no scalar fluxes out from the system during diffusion. The resulting profile is finally computed using the tridiagonal matrix algorithm.

For finely resolved RANS grids and LEM domains, the simulations demand longer computational times which may become impractical for the scope of this work, even if LEM3D scales better with increased complexity than for example DNS simulations. The solution to this became to parallelise the code such that the LEM computations could be distributed over several nodes, thereby drastically reducing the computational time of a simulation. The initialisation and post processing of the code would still be executed sequentially, but the heaviest part of the simulation should ideally be reduced to an $n-1$-th of the original computational time, with n being the number of nodes to be used by the code. This neglects run times of sequential code and intercommunication between nodes which are major factors.

Parallelisation demanded much reworking and analysis of the code, but the work was

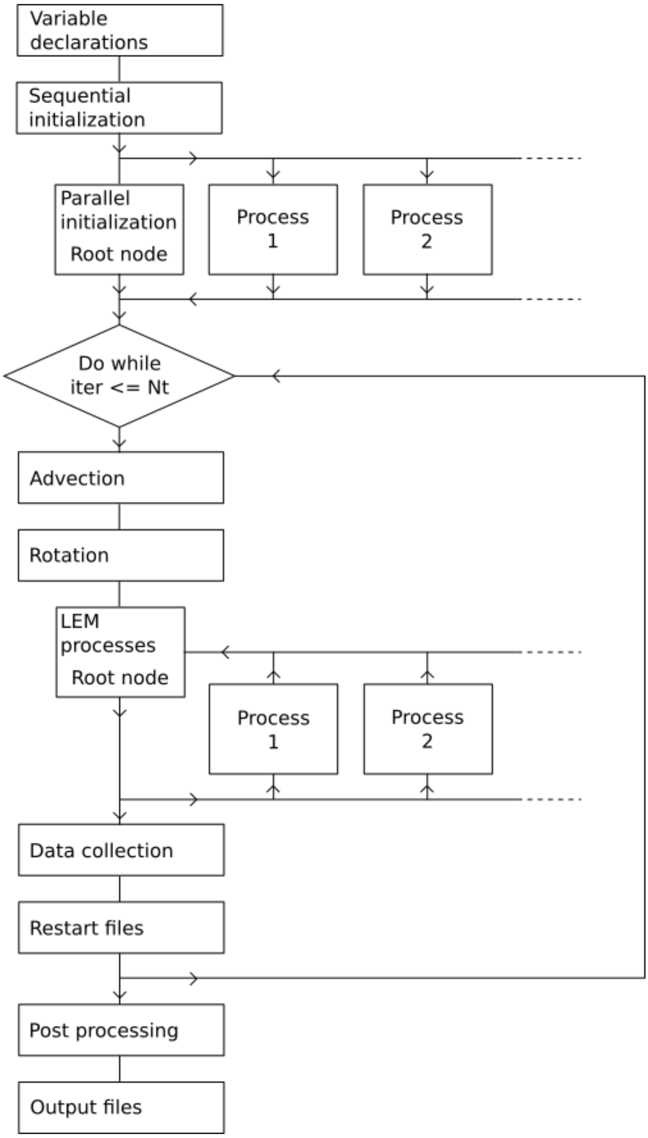

Figure 3.1: An illustration of the code flow, roughly organised in the sequential initialisation, the main loop and the sequential post processing. The parallel computations take place in connection to the LEM processes in the main loop, where all LEM domains are distributed to the parallel processes before the iteration is finished. Iter is the iteration index, and Nt is the set number of iterations for the main loop.

made considerably easier by comparing the code structure to a different implementation of LEM3D which was already parallelised. Most of the subroutines handling parallelisation could be reused with varying degrees of modification.

The first step was to determine what parts of the code would stay sequential, and how to adapt the main time iterations for parallel handling of the LEM domains. The sequential part of the code would be handled by the root thread, while it would distribute 1D LEM domains to be worked on by other threads simultaneously. To keep the processes synchronised, MPI barrier commands were placed at critical points in the code, for example after initialisation such that all variables would be initialised before any threads could start any computations. Similarly, a barrier was placed after each time iteration such that all threads would always work on the same time step.

Parallelisation was implemented such that one root node would run through all LEM domains in the RANS domain, and distribute them to available and idle processors after advective and rotational processes had been performed sequentially. The receiving processors would then perform diffusion and triplet map calculations, since it lies within the confines of the LEM3D that the processes can be performed independently of all other 1D LEM domains. The receiving processes would pick random numbers to determine location, magnitude and times at which the triplet map rearrangements would take place, and perform diffusion of scalar arrays in between each event. Finally, the processed LEM domain would be returned to the root node which would incorporate it into the arrays keeping track of the scalar fields.

The original LEM3D code was written exclusively in Fortran 77. The original idea was to update the code to Fortran 90 since dynamically allocated arrays were not introduced until this version. The version change would also allow the use of modules which would increase the readability of the code and make it more structured. Then all subroutines concerning parallelisation could be moved to modules. This was thought to be necessary at first and quite some time was spent on this implementation, but it was aborted after it was discovered that the passing of allocatable arrays as subroutine arguments introduced some compilation errors which would be quite time consuming to correct.

Instead, the code was rewritten to only handle statically defined arrays. Using only static arrays caused the need for more arrays than was originally necessary to be defined, which caused higher memory requirements. However, it was observed during run time that this was so minimal that it caused no problems with regards to system memory capacity, at least for small RANS input meshes. The code was kept written in Fortran 77, with a couple of Fortran 90 features which were accepted when compiling using the Fortran 77 compilation wrapper *mpif77*. Otherwise, to avoid allocating any arrays dynamically the number of processes to be run would have to be hard-coded into the source code as a parameter in the variable declaration. A rough outline of the code structure after completed parallelisation can be seen in Figure 3.1.

The new code had to be properly tested before any real simulations could be performed. To make sure that this would not be to time consuming a simple test case for a $22 \times 11 \times 11$ RANS domain, with a square jet inlet of 0.4×0.4 cm^2 was set up using ANSYS Fluent. The 1D LEM resolution was set to 30 wafers per 3DCV. Validation of the parallelisation would happen by comparison to results by the sequential code. The parallelisation of the code would cause the random numbers to be picked in a different order than the sequential code, since each 1D LEM domain is assigned its own set of random number generating seeds. The sequential code shares a set of two seeds between all domains and therefore the instantaneous triplet map events will be very different between the two codes due to architecture and hardware factors coming into play when it comes to which thread acts first. However, the two programs should converge to the same solutions when a sufficient amount of statistics has been collected. Despite this, the sequential code was modified to give each LEM domain an independent set of seeds, which allowed testing for only a few iterations at a time.

Due to errors in the parallelisation, extensive debugging was necessary before the testing yielded results agreeing with the original code. Both codes were run on two different systems, and for one system the parallel code was observed to be slower than the sequential code, by a slowdown of 4 minutes, or nearly 12%. The other pair of test runs performed on different hardware experienced a similar 4 minute extended run time for the parallel code. The parallel code was run on 4 processors including the root node, and therefore it was assumed that computational time would be decreased. However, the test case had a very low resolution which would likely cancel out the benefits of the parallelisation due to the added work from communication between processes, and higher resolution of the LEM domains should reverse this effect. In other words, a finer LEM resolution should increase the cost saving effect. Some nodes on the NTNU cluster used for simulations only had 4 processors available, which was the reason for this early test case. The extent of the performance increase from parallelisation would be difficult to predict because of the resolution scaling and since parts of the time iterative loop was still computed sequentially, so this would have to be investigated by even more test runs.

3.2 Using the Software Tools

The LEM3D is dependent on being provided initial data externally, and cannot initialise itself. Therefore, initial data must be provided by other software, in this work ANSYS Fluent was chosen to prepare a Cartesian grid and compute a steady flow velocity field and turbulent properties for the three-dimensional domain. In the end of the section other tools and use of the LEM3D code are presented as well.

3.2.1 ANSYS Fluent

ANSYS [23] is a commercial collection of software providing numerical solution in a variety of scenarios and scopes, be it mechanical, construction or fluid mechanical engineering. Fluent is a CFD tool solving flow problems in even complex geometries and for turbulent cases, and provides a variety of options in terms of computational solution schemes. The grids were designed to be cuboids, or rectangular prisms, using the ANSYS Geometry and Mesh components. An illustration of the grids can be seen in Figure 3.2, and the jet inlet is placed at the centre of the quadratic face which is in view. Two grids were prepared, one of $23 \times 23 \times 38$ cells, and one of $69 \times 69 \times 114$.

In order to ensure exact cubic cells in the grid, the length, width and height scales were all adjusted to allow for this, while creating a domain large enough such that the walls may be treated to be infinitely far away and wall effects can be neglected. However, to keep the Cartesian grid from deforming near the jet inlet, the circular jet inlet was instead modelled as a square inlet. The diameter $D_j = 0.53$ cm of the circular inlet was taken into consideration and a square inlet of the equivalent area was used, see Figure 3.2. The edge length of this inlet would the be used to determine the size of all cubic cells in the mesh as this was a suitable working scale. For the finest grid the cell face areas are nine times smaller than for the coarsest mesh, and hence the inlet consists of a 3×3 grid of cell faces for this mesh.

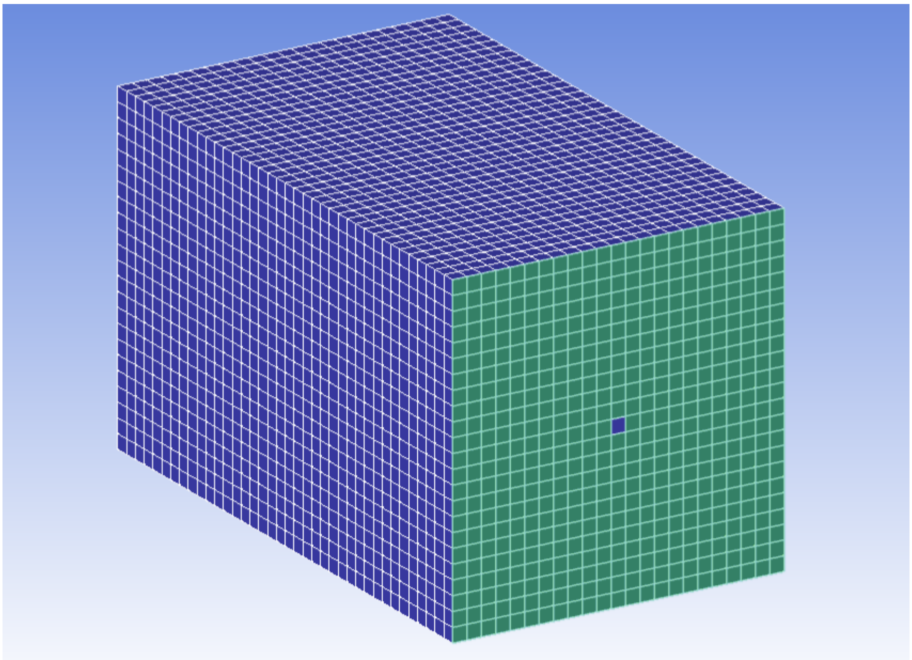

Figure 3.2: The 3D mesh displayed with the inlet shown at the center of the square surface.

The prepared grids were loaded into Fluent to compute solutions for different mixtures. Boundary conditions were set such that the side walls were treated as pressure inlets, as was the face containing the inlet. The surface of the grid opposite to the inlet was defined as a pressure outlet. For computational methods, second order upwind methods were chosen whenever applicable. The k-ε turbulence model was chosen with slightly tuned parameters. $C_{1\varepsilon}$ was chosen to be 1.44, while $C_{2\varepsilon} = 1.83$, since this would give a more correct spreading and jet width compared to experiments, as used by Sannan et al. [16].

The properties of the mixtures were chosen in order to ensure that minimal differential diffusion was introduced in Fluent. This matter would be left to the LEM3D to ensure that differential diffusion is isolated to the solution computed by the LEM, and then it is easier to evaluate how well, or how accurately the LEM predicts differential diffusion compared to other data. The different elements and substances were defined one by one and were eventually combined in mixtures. The H_2/Freon 22 ($CHClF_2$) mixtures were set to be governed by (ideal gas) mixing laws such that all species would have equal diffusive properties, as is traditionally assumed for many turbulent flows. This would therefore assure that no differential diffusion would take place in the Fluent simulation. Thermal diffusion was neglected since all initial conditions were set to the same temperature of 298 K.

The faces of the domain were defined as pressure inlets and outlets, except for the jet inlet which is a velocity inlet with the boundary condition $U_{\mathrm{jet}} = 73$ m/s. Standard conditions for temperature, $T = 298$ K and gauge pressure equal to zero were applied to the domain boundaries. The turbulent intensity was set at 5% while the turbulent length scale was chosen to be 0.1 cm. The stopping criterion for the simulation was defined to be that the absolute magnitude of the continuity equation residual would fall below 10^{-6}.

After running the simulation for 2000 iterations and obtaining a steady-state solution, multiple lines were defined in the domain. The lines were drawn from the central symmetry axis and in the horizontal plane towards the edges of the boxed domain, becoming radial lines and orthogonal to the jet center axis, see Figure 3.3. The velocities parallel to the jet center axis along the cells on the radial lines were stored in data files and further processed in other software. This was done by plotting the interesting data and then enabling it to be written to file. The radial lines were plotted at points along the center axis at fixed distances as close as possible to an integer number of inlet diameters. Using these, the jet half widths and the spreading rate of the jet could be computed. The half width is here the radial distance from the jet centerline at which the streamwise velocity component is half the value of the velocity exactly at the centerline.

In the Maple software, scripts were written to process the radial lines, an example of which is displayed in Figure 3.4. Using simple algorithms the half width of the jet at the end of the domain is determined. The velocity profile could then be investigated in closer detail, and revealed that the Fluent solution is not perfectly symmetric. When extracting velocity and turbulent data from Fluent, UDFs would be used which will be described in the next section. However, when computing the integral scale based on the turbulent properties several incorrect, high magnitude values would appear outside the jet near the inlet end. This is illustrated in Figure 3.6 and will be described in more detail later, but illustrates that the Fluent solution has its drawbacks.

A second jet configuration was also treated using ANSYS Fluent, and subsequently LEM3D. Differences to the previous case lies in the jet mixture as well as the boundary conditions. This new scenario treats a jet mixture consisting of 36% H_2 complemented by 64% CO_2, measured in mole fractions. In addition, the jet is now placed at the exit of a wind tunnel such that the surface of the computational domain where the jet inlet is located has an incoming air co-flow at a speed of 1.5 m/s. The co-flow is illustrated in Figure 3.5.

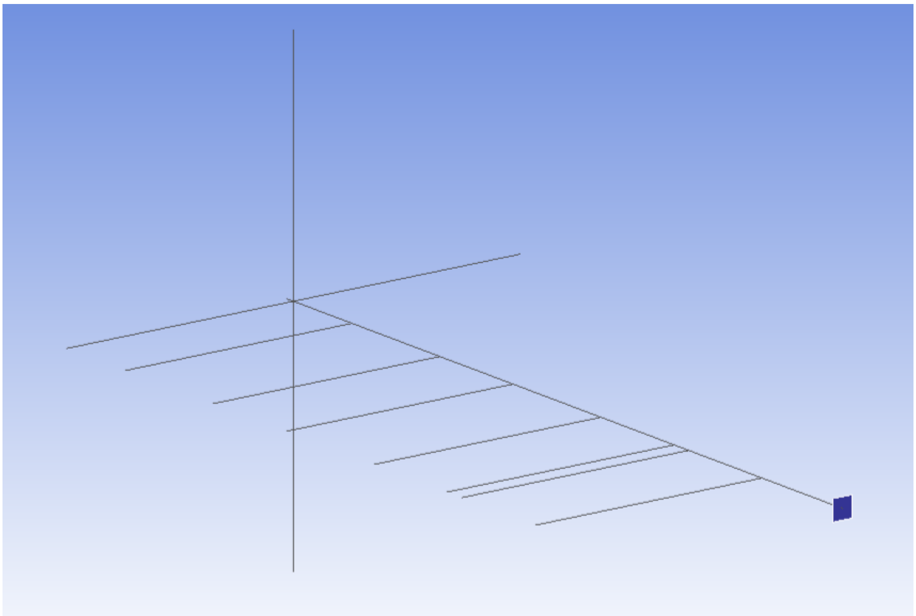

Figure 3.3: The radial lines defined within the mesh shown in relation to the jet center axis and the square inlet.

The jet diameter is in this case set to $D_j = 0.77$ cm.

The computational domain had to be resized in order to capture the entire length of the new jet, the initial setup was 23 × 23 × 70 3DCVs with edge lengths of 0.6824 cm. The case needed to be recomputed for 6 distinct Reynolds numbers between 2000 and 64000, corresponding to inlet velocities in the range $U_{\text{jet}} = 3.4$ - 108.8 m/s. Unfortunately, the solution would suffer similar irregularities and boundary effects as the integral scale data in Figure 3.6, only in the opposite end of the domain. The UDFs used in the previous case could be also applied to remove these effects, but the jet turbulence would widen for higher Reynolds numbers and grow outside the domain eventually. In the interest of keeping the computational domain and computational time as small as possible, the domain width and height was incremented in steps of 2 until a suitable solution was reached. In the end, this approach ended in a RANS mesh of $33 \times 33 \times 70$ for $\text{Re} = 16000, 64000$, and $41 \times 41 \times 70$ for $\text{Re} = 32000$. The $\text{Re} = 32000$ case proved difficult to find, since the edge effects were quite prominent within the jet itself, which meant the domain width would have to be increased even more to find a clean solution. However even so, the cleaning algorithm failed to remove only the edge effects, but also removed the integral scale far downstream from the jet itself. At first the width was increased step wise to 59 such that the edge effects would be far removed from the jet, but ANSYS Mesh failed to create perfect hexagonal meshes for configurations wider than 43 cells. The wider meshes were also tested with other versions of ANSYS on different hardware. After some additional analysis of the algorithm cleaning the data, it was discovered that by tuning a few param-

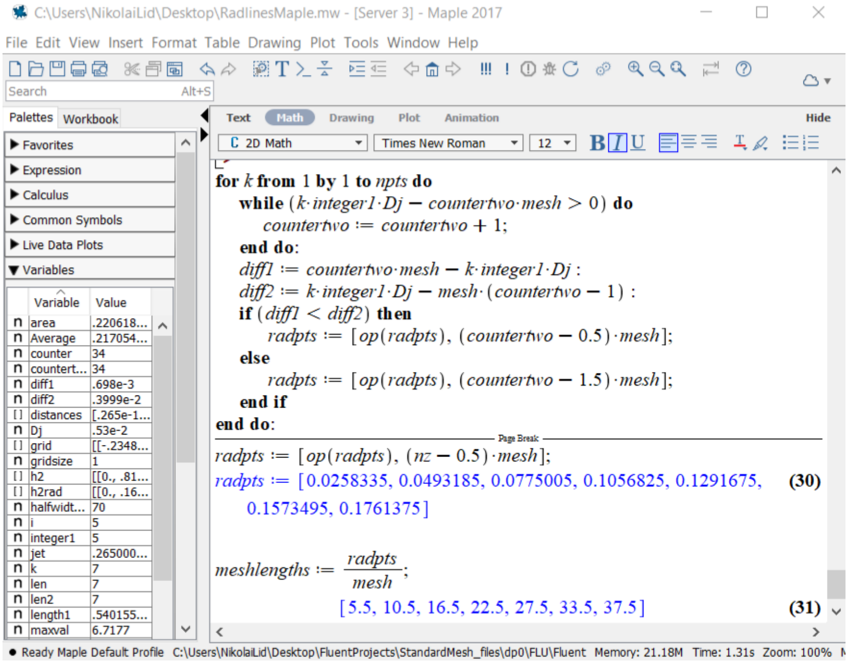

	Variable	Value
n	area	.220618...
n	Average	.217054...
n	counter	34
n	countert...	34
n	diff1	.698e-3
n	diff2	.3999e-2
[]	distances	[.265e-1...
n	Dj	.53e-2
[]	grid	[[-.2348...
n	gridsize	1
[]	h2	[[0., .81...
[]	h2rad	[[0., .16...
n	halfwidt...	70
n	i	5
n	integer1	5
n	jet	.265000...
n	k	7
n	len	7
n	len2	7
n	length1	.540155...
n	maxval	6.7177

```
for k from 1 by 1 to npts do
    while (k·integer1·Dj − countertwo·mesh > 0) do
        countertwo := countertwo + 1;
    end do:
    diff1 := countertwo·mesh − k·integer1·Dj :
    diff2 := k·integer1·Dj − mesh·(countertwo − 1) :
    if (diff1 < diff2) then
        radpts := [op(radpts), (countertwo − 0.5)·mesh];
    else
        radpts := [op(radpts), (countertwo − 1.5)·mesh];
    end if
end do:
```

```
radpts := [op(radpts), (nz − 0.5)·mesh];
radpts := [0.0258335, 0.0493185, 0.0775005, 0.1056825, 0.1291675,      (30)
    0.1573495, 0.1761375]
```

```
meshlengths := radpts / mesh;
                 [5.5, 10.5, 16.5, 22.5, 27.5, 33.5, 37.5]                (31)
```

Figure 3.4: The final part of a script made in Maple, designed to analyse some of the data from the Fluent output.

eters the 41-width solution would suffice anyway, and hence all the relevant cases were readily prepared for LEM3D simulations. It must be noted that the Fluent solution for a jet of Reynolds number 1000 was only very weakly turbulent, and the resulting turbulence data profiles were poorly resolved and not very smooth as a consequence. A decision was made to only continue with the cases for $\mathrm{Re} = 2000$ and above.

Finally, the process used to find stable Fluent solutions for LEM3D input can be summarised in the following steps,

1. Create geometry
2. Create hexagonal mesh
3. Compute steady-state RANS solution in Fluent
4. Extract velocity profile data, and compute jet half width in Maple
5. Create jet property output files using UDFs
6. Correct integral scale data using UDFs
7. Compile LEM3D code, and tune run parameters according to test-run output
8. Run LEM3D simulation and analyse results

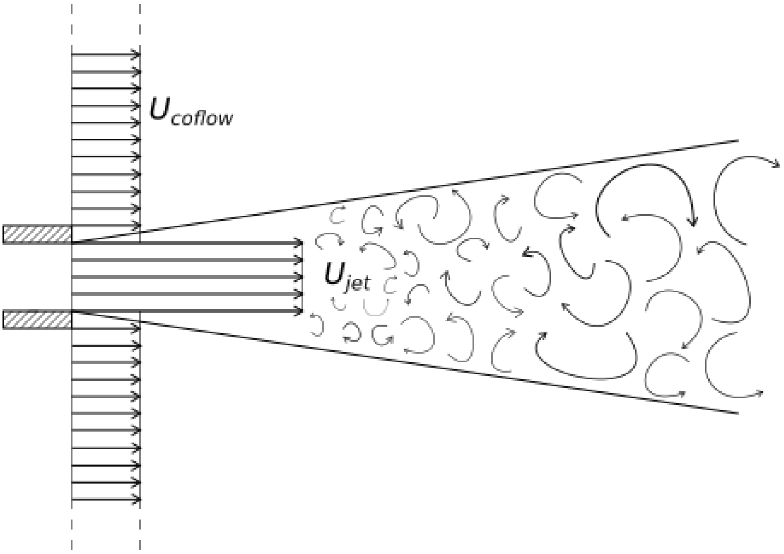

Figure 3.5: A turbulent jet cross section containing the jet center axis. The turbulent eddies are depicted as simple curves, while the inlet and co-flow velocities, U_{jet} and U_{coflow} are depicted as uniform velocity fields. The walls of the inlet are assumed to be infinitely thin.

3.2.2 Preparing Input Data for LEM3D

Through the use of User Defined Functions (UDFs) in Fluent, the generated data was formatted and written to file, using a coordinate formatting setup created in Maple. The UDFs were written in the C programming language, and were provided by SINTEF. The UDFs create input files for LEM3D for the quantities; turbulent diffusivity (D_{T}), modified integral scale (L_{mod}), molecular viscosity (ν), and all three velocity components. In particular, the integral scale was computed using other turbulent quantities by way of Equation (2.20). The corresponding input-files needed for a LEM3D run are listed in Table 3.2.

Parameter	**Description**
jet_u_velocity.dat	The streamwise velocity component of the jet, in units [cm/s].
jet_vj_velocity.dat	The lateral jet velocity in the j-direction, in units [cm/s].
jet_vk_velocity.dat	The lateral jet velocity in the k-direction, in units [cm/s].
jet_diffusivity.dat	The turbulent diffusivity, D_{T}, in units [cm^2/s].
jet_viscosity.dat	The molecular viscosity, ν, in units [cm^2/s].
jet_integralscale.dat	The modified integral scale, $L_{\mathrm{mod}} = c\Lambda$, in units [cm].

Table 3.2: The input files required to run LEM3D, and their descriptions.

MatLab scripts were written in order to plot and investigate the different input data. The integral scale in particular was investigated and proved that the data contained some inaccuracies, which justified cleaning parts of the data files to prevent errors. The inaccurate data was mainly due to round-off errors when dividing k and ε for small values, which caused large spikes in the resulting output. A UDF was used especially for the cleaning operation and ensured that the integral scale was negligible in the non-turbulent flow part of the domain. Examine Figure 3.6 to see an example of cleaned versus uncleaned data. Spatial gradients in the integral scale distribution were investigated and used to lessen the unphysical integral scale values.

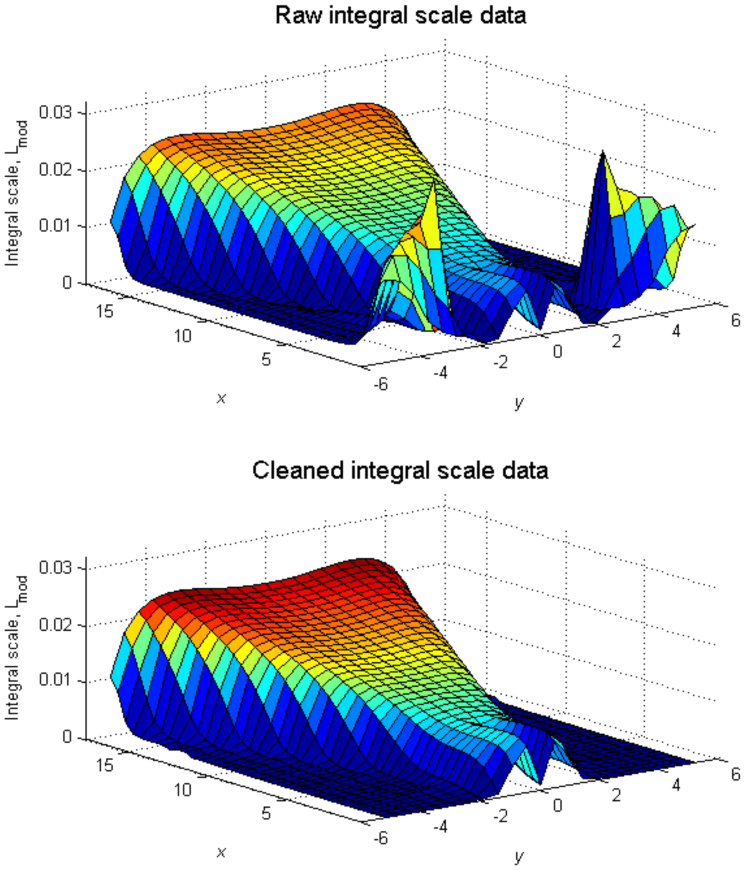

Figure 3.6: Comparison of the cleaned integral scale data in a horizontal plane containing the jet center axis, to the untreated data. Spatial coordinates are in units cm, while the integral scale L_{mod} is given in units m.

Maple was, as mentioned, used to calculate the half width of the jet at the end of the domain which was used as a scaling factor for the values of the resulting integral scales. This was done in Fluent by extracting streamwise velocity components at the end of the RANS domain, as illustrated in Figure 3.3.

The fine and coarse meshes each served as the source of input for two separate series of simulations. A third set of simulations was based on input created by averaging the fine mesh solution, and modifying the number of cells such that the modified solution was adapted to a Cartesian $23 \times 23 \times 38$ mesh matching the coarsest solution. For the velocity components, the material flux over the finely resolved cell faces corresponding to a coarsely resolved cell face was used to compute the modified velocity. The integral scale, turbulent diffusivity, and viscosity are computed by averaging the 27 cell values which constitute one modified cell. Thus, three sets of input data was generated; a finely resolved set, a modified set, and a coarsely resolved set for the H_2/Freon 22 jet.

The general procedure described in this subsection was also applied to the CO_2/H_2 jet, apart from the modified mesh approach. Only that in these cases, the inlet velocity was varied in order to create RANS solutions for different Reynolds numbers.

3.2.3 Using the LEM3D Code - Input Parameters

A set of input parameters would have to be specified to run the LEM3D code. These parameters were set in the input files **jet_init.dat**, **jet_physical.dat** as well as some parameters set directly in the source code. The source code parameters were necessary because of Fortran 77 restrictions. The files with parameter explanations can be found in Tables 3.3 and 3.4, while the source code parameters can be seen in Table 3.5. The parameters for the position, and configuration of a thermal source downstream in the jet are included in the files, but they were deactivated by setting isrc = 0, for all simulations referred to in this document.

Parameter	Description
Ni	Number of 3DCVs in the x-direction.
Nj	Number of 3DCVs in the y-direction.
Nk	Number of 3DCVs in the z-direction.
srcloc	The x-axis index of the 3DCV where a thermal source is located.
RANSdx	The length of a cubic 3DCV.

Table 3.3: The parameters specified in the **jet_init.dat** input file, and their descriptions.

Some parameters are subject to certain restrictions. For instance, the CFL number must be less than $\frac{2}{3}$ in order for the code to run. Another necessary requirement is that the LEMres has to be an even number. Otherwise, the input parameters from files has to be within the corresponding limit parameters set in the source code, as for example Ni,

Parameter	Description
Nt	The number of iterations at the RANS advection time scale.
datcst	The number of iterations before data collection starts.
datmod	The number of iterations between each time statistics are collected for scalar profiles.
varmod	The number of iterations between each time statistics are collected for scalar profiles along centerlines in j- and k-direction.
velmod	The number of iterations between each time the average number of LEM wafers crossing 3DCV surfaces are computed.
LEMres	The resolution of a 1D LEM domain per 3DCV length.
CFL	The Courant-Friedrichs-Lewy number.
rad(1)	The radius of one ring shaped, co-centric thermal source.
rad(2)	The radius of another ring shaped, co-centric thermal source.
DfM(1)	The molecular diffusivity of scalar species 1.
DfM(2)	The molecular diffusivity of scalar species 2.
PrT	The turbulent Prandtl number.
lkfac	A factor determining how closely the Kolmogorov scale should be resolved.
rotfac	Parameter affecting the frequency of rotations for 3DCVs.
loc(1)	The first downstream center axis position where differential diffusion is computed.
loc(2)	The second downstream center axis position where differential diffusion is computed.
loc(3)	The third downstream center axis position where differential diffusion is computed.
loc(4)	The fourth downstream center axis position where differential diffusion is computed.
loc(5)	The fifth downstream center axis position where differential diffusion is computed.
loc(6)	The sixth downstream center axis position where differential diffusion is computed.
locx	A jet center axis position far downstream used to determine the maturity of the solution.
isrc	A flag activating point or ring shaped thermal sources in the jet flow.
comp	A flag activating compression of the triplet maps, keeping their length confined within a 3DCV.
restrt	A flag indicating whether the initiated run is a restart of a previous simulation or not.
rstmod	The number of iterations between updates of restart files.

Table 3.4: The parameters specified in the `jet_physical.dat` input file, and their descriptions.

Name	Version(s)
NSCMAX	The maximum number of scalar fields allowed in the simulation.
LOCMAX	The maximum number of output locations for differential diffusion results.
ProcNumber	The number of processes used when running the code.
LMXMAX	Parameter setting a maximum eddy length for triplet maps.
RESMAX	The maximum 1D LEM domain resolution.
IMAX	The maximum number of 3DCVs in the streamwise i-direction.
JMAX	The maximum number of 3DCVs in the lateral j-direction.
KMAX	The maximum number of 3DCVs in the lateral k-direction.
RMAX	The maximum number of 3DCVs in the lateral radial direction.
varMAX	The maximum number of variables allowed in the mean fields.
velMAX	The maximum number of variables in the velocity fields.
lmaxmx	Parameter setting the maximum length for triplet maps, which cannot be larger than LMXMAX.
kmin	The smallest allowed size of a triplet map is 3 × kmin LEM wafers.
Nscalr	The number of distinct scalars in the simulation.
Nlocs	The number of downstream locations for differential diffusion output.

Table 3.5: A list of parameters declared and initialised directly in the source code.

Nj, and Nk are to the set of IMAX, JMAX, and KMAX. Similarly, lmaxmx mus be less than or equal to LMXMAX, but the code has some built-in tests which will recommend new values for these parameters if they are too small judging by integral scale data input. Similar tests exist for most input parameters, even the data collection parameters datcst, datmod, varmod, and velmod are subject to such tests. This helps make the code considerably more user friendly, despite having to set some parameters in the source code, and recompiling every time they are tuned.

The ProcNumber parameter needs to match how many processors the code is set to run on, when entering the code execution command. Hence recompilation is necessary for each change of processor numbers. The lkfac is another crucial parameter, which bounds the size of the smallest resolved eddies. lkfac = 1, would give eddies resolved all the way down to the Kolmogorov scale, lkfac = 2 would give smallest eddies twice the length of the Kolmogorov scale, and so on.

The loc-positions were set according to the ratio $x/D_j = \mathrm{pos}$, i.e., a number of jet diameters along the jet center axis since this is a common measure when considering jets. To find the correct 3DCV index i for the computational domain, the formula

$$i = \frac{\mathrm{pos}\,\mathrm{D_j}}{\mathrm{RANSdx}} + \frac{1}{2},$$

was used. Normally, this would yield a non integer, and hence the closest integers above and below this value would be entered in the loc list, such that the solution at the correct position could be reached by weighted interpolation.

The final parameter configurations used for the simulations presented in the results section are listed in Appendix B.

3.2.4 Post-processing

Within the code there is a section handling post processing of data which is mainly concerned with computing statistics, such as means, variances, and correlations, while writing the scalar fields and differential diffusion results to output files.

Some additional post-processing was sometimes needed. Because of the limited RANS resolution, the location of output data along the jet centerline is somewhat poorly resolved. Therefore, to find output at specific locations along the jet center axis, some interpolation between lateral profiles was necessary. It was deemed sufficient to use linear interpolation in stead of higher order methods, since more values along the jet axis for higher order interpolation would increase the computational work and make it more cumbersome to treat output data. A piece of MatLab code interpolating and plotting profiles is displayed in Appendix C.

3.3 Simulation Procedure

The input values used for the different parameters in **jet_init.dat** and **jet_physical.dat** can be seen in Tables 3.6 and 3.7. The molecular diffusivities were set according to Sannan et al. [16] and Massman [24], for the two different mixtures.

Parameter	**Description**
Ni	23, 33, 41, 69
Nj	23, 33, 41, 69
Nk	38, 70, 114
srcloc	0
RANSdx	0.1566, 0.4697, 0.6824

Table 3.6: The parameters specified in the **jet_init.dat** input file, and the value ranges used for simulations.

At first, different sets of simulations were determined to run. For a RANS mesh of $23 \times 23 \times 38$ 3DCVs, the LEM resolutions 128, 256, 512, 1024 with lkfacs 8, 4, 2, and 1, respectively, was used. Similarly, for the RANS mesh $69 \times 69 \times 114$ simulations with LEM

Parameter	Description
Nt	50000
datcst	20000
datmod	50
varmod	100
velmod	1000
LEMres	42, 84, 90, 100, 128, 140, 256, 512
CFL	0.1
rad(1)	0.1
rad(2)	0.1
DfM(1)	0.77
DfM(2)	0.12, 0.14
PrT	0.7
lkfac	8, 4, 2
rotfac	1.0
loc(1)	11, 17, 34
loc(2)	12, 18, 35
loc(3)	23, 34, 68
loc(4)	24, 35, 69
loc(5)	34, 68, 102
loc(6)	35, 69, 103
locx	35, 69, 105
isrc	0
comp	0
restrt	0, 1
rstmod	5000

Table 3.7: The parameters specified in the **jet_physical.dat** input file, and their value ranges used in simulations.

resolution 42, 84, and 168, using lkfacs 8, 4, and 2, respectively, was employed. These LEM resolutions denote the number of LEM wafers in 1D per 3DCV edge length. The resolutions for the finest mesh are therefore approximately equivalent to the more poorly resolved RANS mesh, since three of the 3DCVs from the finest mesh, are as long as one of the 3DCVs from the other. Parallelisation of the source code for the LEM3D model was applied, but the computational time limitations was still far too large for the scope of the present work for the finest LEM resolution. Problems were also encountered with regards to RAM requirements for highly resolved RANS meshes with finely resolved LEM domains. Therefore, the LEMres = 1024, 168 with lkfac = 1 simulations were aborted.

The first steps to start a simulation were to determine the output locations for differential diffusion, and different axis diameter scalings were taken into consideration. Next, all necessary input data was determined by way of looking up the correct data, and comparing parameters to other papers with subsequent result comparison in mind.

Input files from Fluent would be supplied as described in Section 3.2.2. The necessary parameters for RANS dimensions and LEM-arrays would then be set in the code, before compiling and doing a short test-run, to get information about recommended maximum limits on triplet map eddy boundaries. Afterwards, all would be ready to run the simulations. The post processing and handling of results have already been described in Section 3.2.4.

In the case of run time interruptions of the simulations, the programme is fortunately written such as to periodically store restart files at certain iteration intervals, controlled by the parameter rstmod. Then by toggling the rstrt flag in the **jet_physical.dat** file, the simulations continue from the previous point restart files were written. The number of iterations Nt must be subtracted by the number of iterations the programme completed before writing the current restart files, otherwise the program run will be extended by a similar number of steps.

For the cases equivalent to the ones treated by Smith et al. [2] and Maragkos et al. [3] a different approach was taken. As Sannan et al. [16] have demonstrated, the LEM3D is strongly dependent upon the LEM resolution, and a high resolution would most likely yield the most precise results. However, to keep the computational time consumption feasible for the scope of the present work, the resolution had to be limited. Test runs were performed for the different values of Reynolds numbers, and since the resolution of this system was coarser than the Freon 22 case, with larger 3DCVs, the LEM resolution would be lower than for the previous jet configuration. A general resolution of 100 LEM wafers per 3DCV, equivalent to a wafer thickness of $6.824 \cdot 10^{-5}$ m was deemed suitable, with individual adjustments for the different Reynolds numbers. A short LEMres refinement was performed for $\mathrm{Re} = 64000$ in order to test the run time dependence.

Manufacturer	**Model**	**# Cores**	**Clock speed** [GHz]
Intel	i7-920	4	2.66
Intel	i7-930	4	2.80
Intel	i7-960	4	3.20
Intel	i7-9530K	6	3.50
Intel	Xeon E5-2630 v4	10	2.20

Table 3.8: The processors of the systems used for executing simulations.

Most of the simulations were performed on hyper threaded quad-core CPUs on a network of Linux operated machines. An overview of the relevant CPUs and properties are displayed in Table 3.8. Note that all except the final processor in the table are hyperthreaded, which mean the can handle two threads per core. Since the computers are shared between multiple users, some room for others had to be left, and most simulations were run on 6 threads, i.e., two cores dedicated to one thread each, and two cores shared between two threads each. However, the most intensive calculation run on the computing system

Idun, operated and administrated by the High Performance Computing Group at NTNU. Then 6 nodes each with two CPUs containing 10 cores each were utilised to speed up the calculation from well over 80 days of computational time to less than 200 hrs. For other simulations that were estimated to last over 21 days, they were also run on Idun, using 2 or 3 nodes, according to what was available at the time.

Chapter 4

Results

Disregarding test simulations and alternative jet configurations, the simulation procedures resulted in 8 Fluent simulations and 13 LEM3D simulations. Their results are presented in this chapter.

4.1 RANS Solutions

The input data created in the ANSYS software is in itself a set of simulation results, and are displayed graphically here.

4.1.1 The H_2/Freon 22 Jet with Resolution $23 \times 23 \times 38$

The streamwise u-velocity component and the turbulent viscosity of the solution for the $23 \times 23 \times 38$ RANS-mesh, using the settings specified in Section 3.2.1, are displayed in Figure 4.1 and 4.2. The inlet velocity is set to $U_{\mathrm{jet}} = 73$ m/s, while the jet Reynolds number is $\mathrm{Re} = 20000$.

The u-velocity can be observed to be slightly asymmetric about the center axis, but the turbulent viscosity is shown to be symmetric.

4.1.2 The H_2/Freon 22 Jet with Resolution $69 \times 69 \times 114$

As in the previous subsection, here the streamwise u-velocity component and turbulent viscosity for the finer $69 \times 69 \times 114$ RANS mesh are presented in Figures 4.3 and 4.4. Compared to the solutions from the previous subsection the velocity values are lower in the region immediately downstream from the inlet, and the maximum turbulent viscosity is half of that for the coarse mesh. The inlet velocity and boundary conditions are the same as for the results in Subsection 4.1.1.

Comparing the finest resolved solution to the same solution averaged and adapted to the rough $23 \times 23 \times 38$ mesh it can be observed that the deviations near the inlet are profound. The finest resolved resolution generally has a higher velocity throughout the chosen domain, and it is fits better with the boundary condition at the inlet in comparison to the modified solution. The velocity profiles are shown in Figure 4.5, and similar differences can be seen for the molecular viscosities in Figure 4.6. However, the turbulent diffusivities from Figure 4.7, which in this figure is the same as the turbulent viscosity divided by the density of the mixture, is a better match, illustrating that the turbulent properties are quite well preserved during the solution modification.

As described in the previous paragraph, the fine mesh solution can be compared to the coarse mesh solution in Figures 4.5, 4.6 and 4.7.

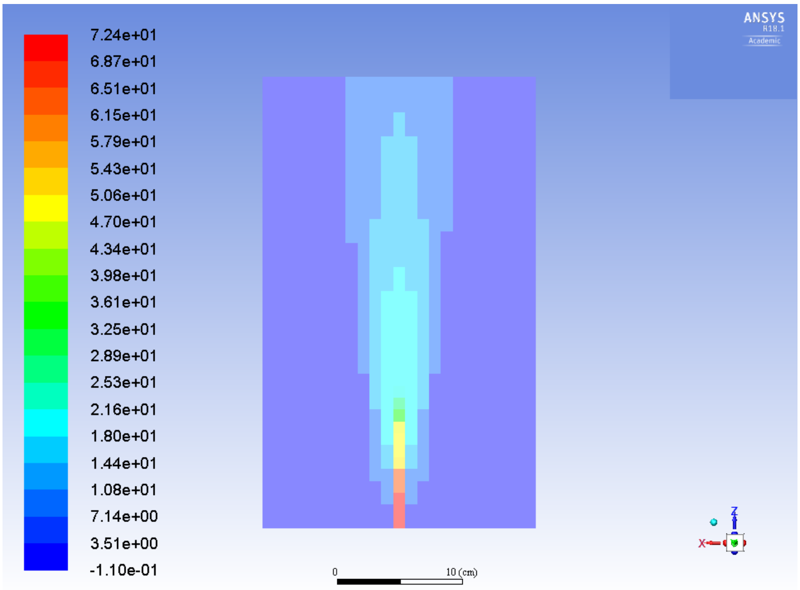

Figure 4.1: A cross section of the jet containing the jet center axis, displaying the streamwise u-velocity component from the Fluent solution for the coarse $23 \times 23 \times 38$ RANS mesh. The scale is in units m/s.

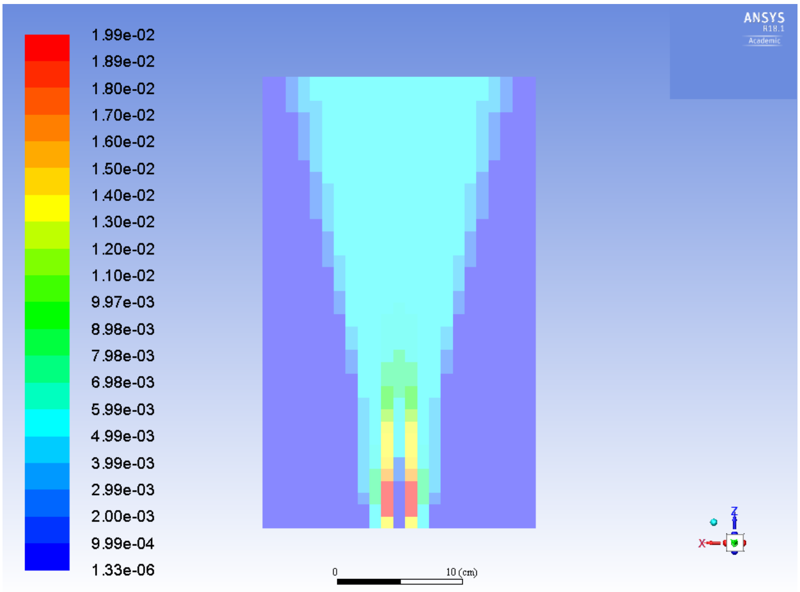

Figure 4.2: A cross section of the jet containing the jet center axis, displaying the turbulent viscosity from the Fluent solution for the coarse $23 \times 23 \times 38$ RANS mesh. The scale is in units kg/m s.

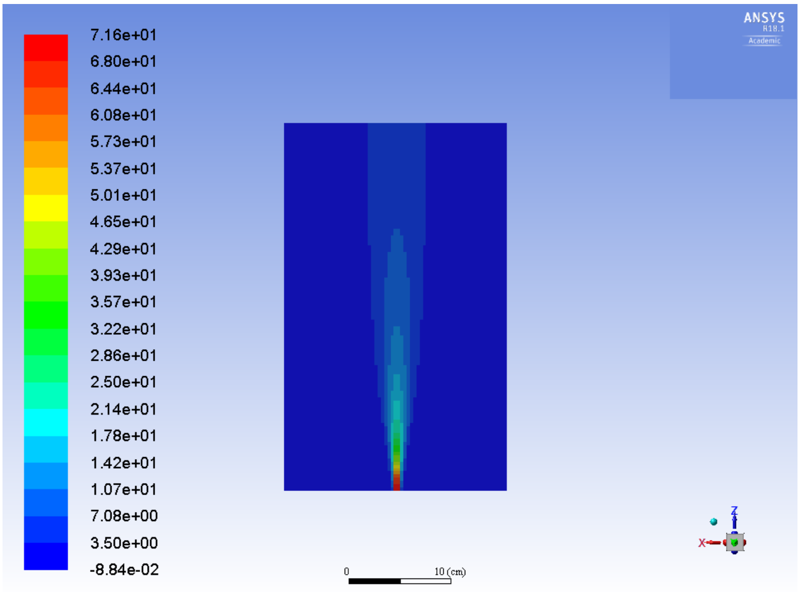

Figure 4.3: A cross section of the jet containing the jet center axis, displaying the streamwise u-velocity component from the Fluent solution for the fine $69 \times 69 \times 114$ RANS mesh. The scale is in units m/s.

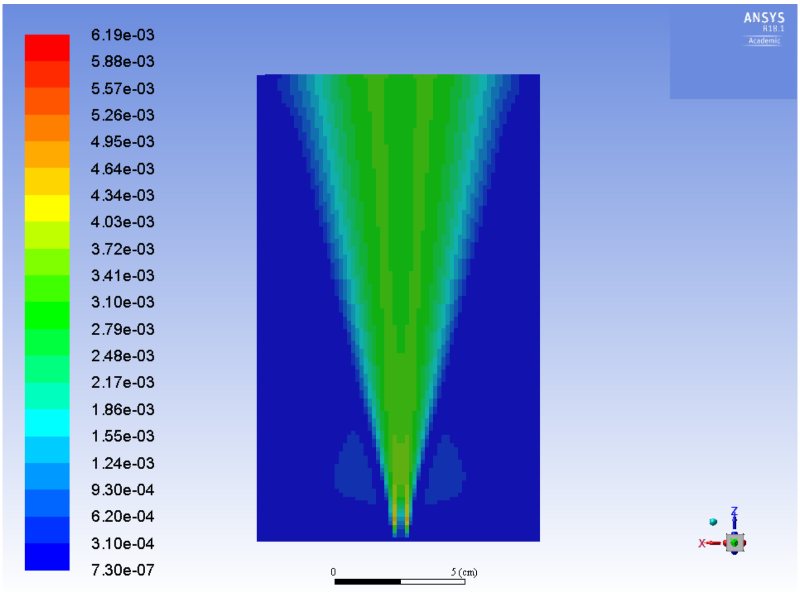

Figure 4.4: A cross section of the jet containing the jet center axis, displaying the turbulent viscosity from the Fluent solution for the fine 69 × 69 × 114 RANS mesh. The scale is in units kg/m s.

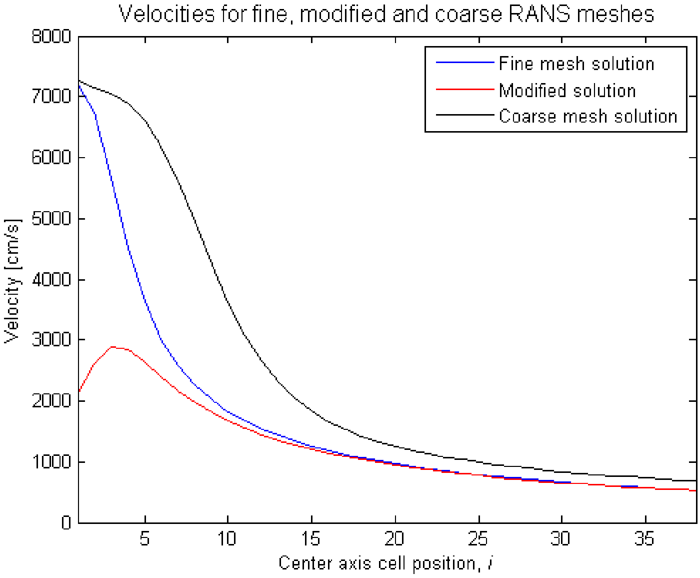

Figure 4.5: The streamwise u-velocities of the finest refined mesh along the jet center axis, compared to the modified solution adapted to a 23 × 23 × 38 RANS mesh, and the direct coarse mesh solution.

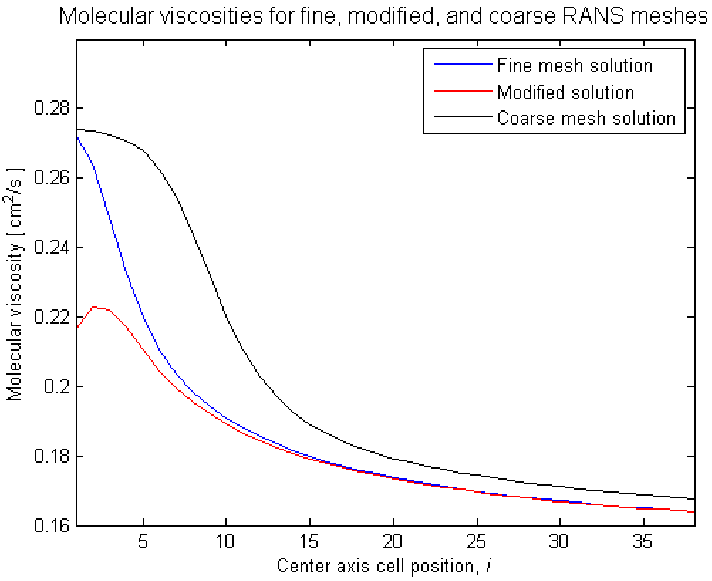

Figure 4.6: The molecular viscosities of the finest refined mesh along the jet center axis, compared to the modified solution adapted to a $23 \times 23 \times 38$ RANS mesh, and the direct coarse mesh solution.

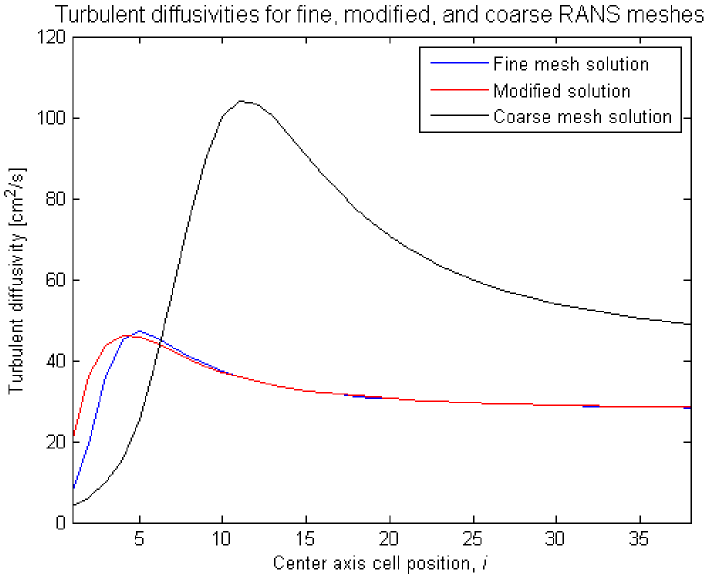

Figure 4.7: The turbulent diffusivities of the finest refined mesh, along the jet center axis, compared to the modified solution adapted to a $23 \times 23 \times 38$ RANS mesh, and the direct coarse mesh solution.

4.1.3 The CO_2/H_2 Jet with Varying RANS Resolution

This section presents the u-velocity, and turbulent viscosity data for different Reynolds numbers for a $64\%CO_2$ and $36\%H_2$ jet, measured in mole fractions. The velocity data in a jet cross section containing the jet central axis for Reynolds numbers 2000, 4000, 8000, 16000, 32000, and 64000 can be seen in Figures 4.8, 4.9, 4.10, 4.11, 4.12, and 4.13. Similarly, the turbulent viscosity is shown in Figures 4.14, 4.15, 4.16, 4.17, 4.18, and 4.19. The inlet velocities corresponding to these Reynolds numbers are $3.4, 6.8, 13.6, 27.2, 54.4$, and 108.8 m/s, and the co-flow incoming in the surface surrounding the inlet has a constant velocity of 1.5 m/s.

The series of velocity profiles reveal that the mean velocity of the jet is more clearly defined for higher Reynolds numbers, and hence the jet is more clearly defined. For the lower Reynolds numbers the co-flow has a larger effect on the jet, and the flow is very close to laminar, only minor turbulent effects are experienced, as seen in the turbulent viscosity plots. The turbulent viscosity figures also display a more well defined jet for higher Reynolds numbers. However, in most of the figures the edge effects can be easily seen in the top right and left corners. None of the profiles seem to be perfectly symmetric, but the $\mathrm{Re} = 32000$ and $\mathrm{Re} = 64000$ profiles are quite close.

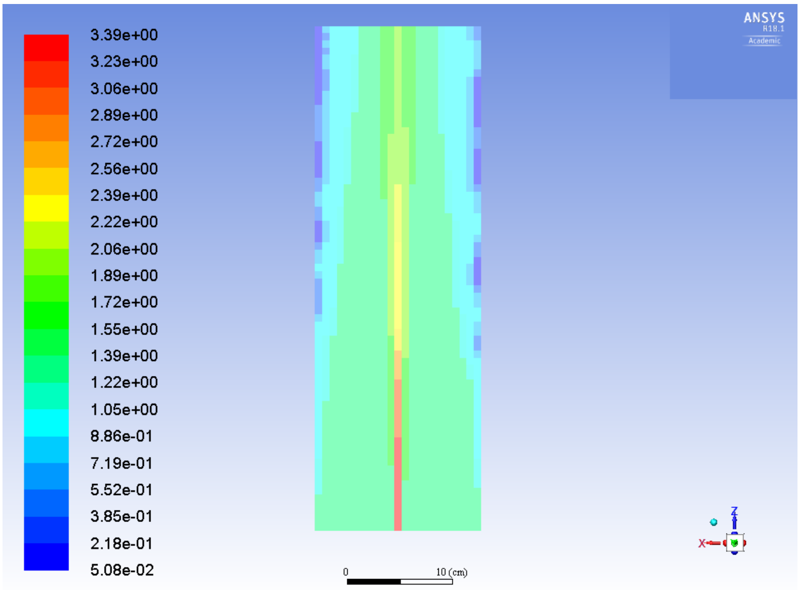

Figure 4.8: A cross section of the $\mathrm{Re} = 2000$ jet containing the jet center axis, displaying the streamwise u-velocity component from the Fluent solution for the $23 \times 23 \times 70$ RANS mesh. The scale is in units m/s.

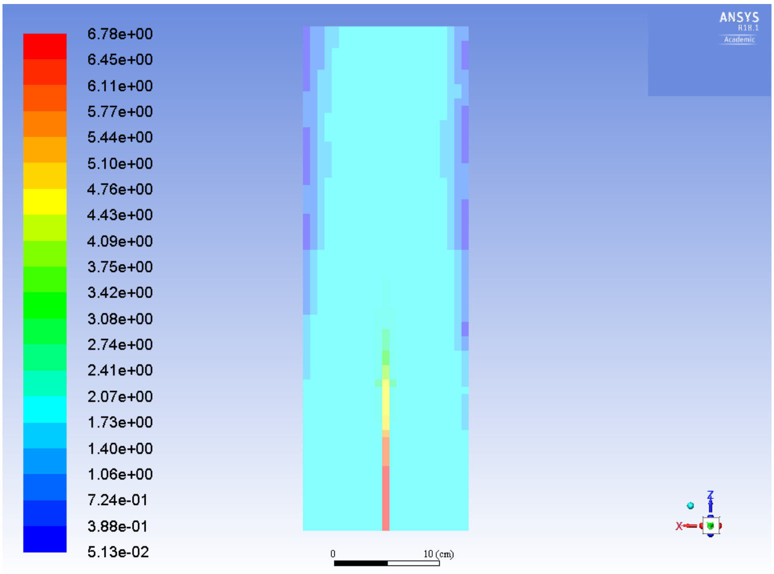

Figure 4.9: A cross section of the $\mathrm{Re} = 4000$ jet containing the jet center axis, displaying the streamwise u-velocity component from the Fluent solution for the $23 \times 23 \times 70$ RANS mesh. The scale is in units m/s.

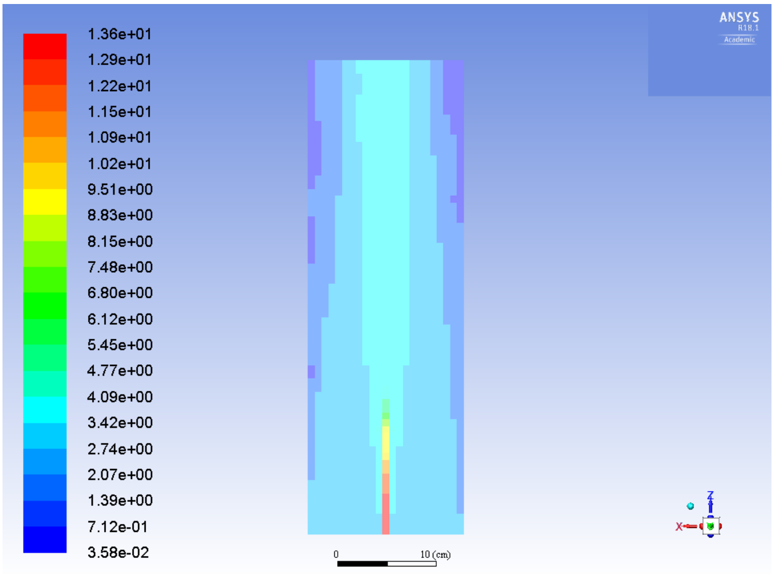

Figure 4.10: A cross section of the $\mathrm{Re} = 8000$ jet containing the jet center axis, displaying the streamwise u-velocity component from the Fluent solution for the $23 \times 23 \times 70$ RANS mesh. The scale is in units m/s.

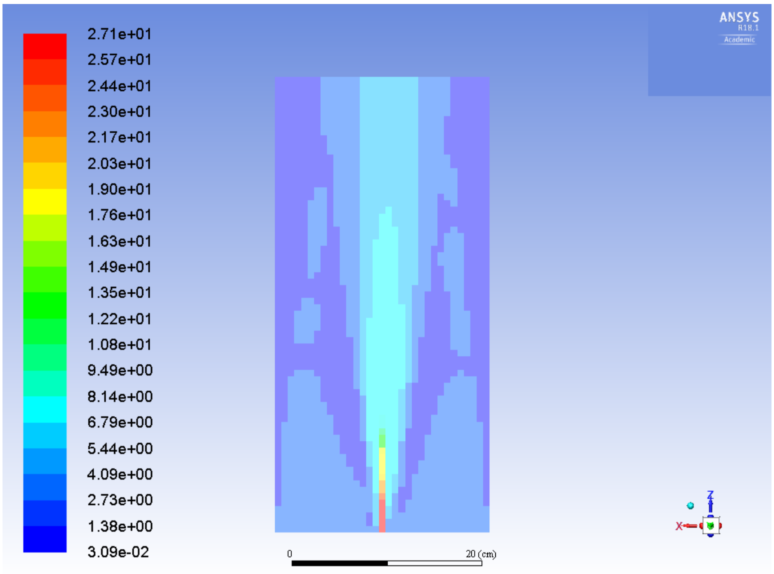

Figure 4.11: A cross section of the $\mathrm{Re} = 16000$ jet containing the jet center axis, displaying the streamwise u-velocity component from the Fluent solution for the $33 \times 33 \times 70$ RANS mesh. The scale is in units m/s.

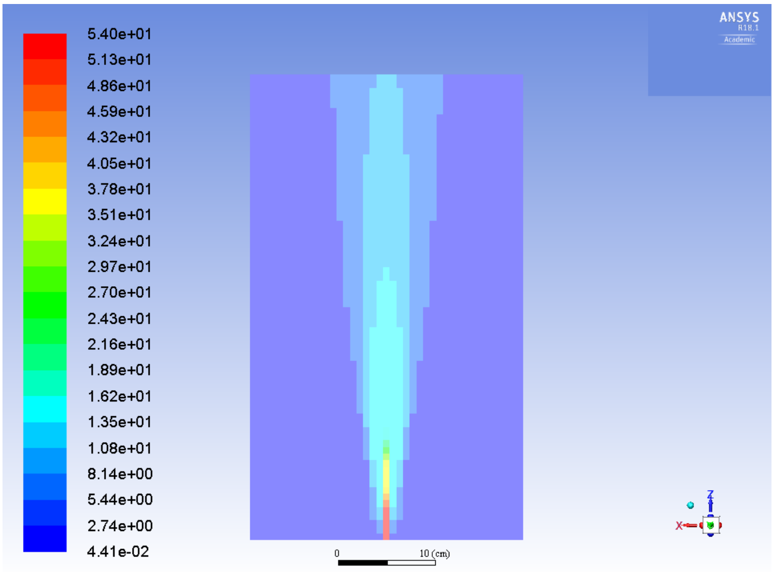

Figure 4.12: A cross section of the $\mathrm{Re} = 32000$ jet containing the jet center axis, displaying the streamwise u-velocity component from the Fluent solution for the $41 \times 41 \times 70$ RANS mesh. The scale is in units m/s.

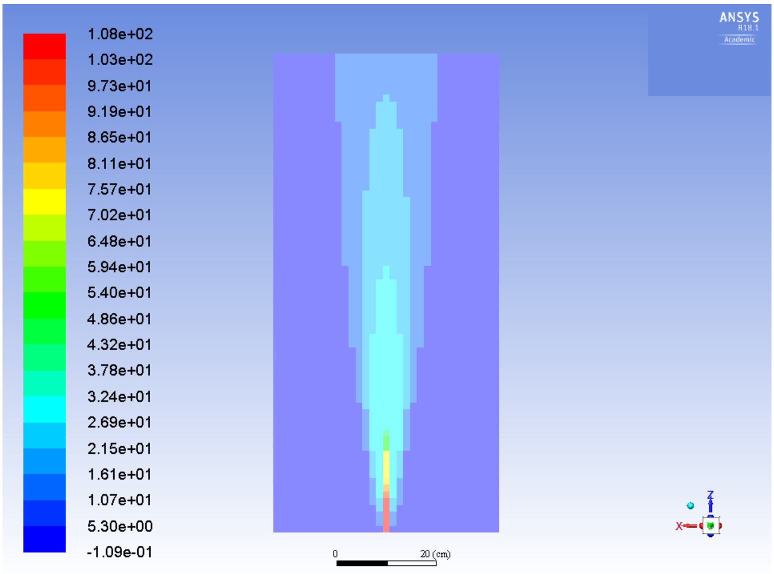

Figure 4.13: A cross section of the $\mathrm{Re} = 64000$ jet containing the jet center axis, displaying the streamwise u-velocity component from the Fluent solution for the $33 \times 33 \times 70$ RANS mesh. The scale is in units m/s.

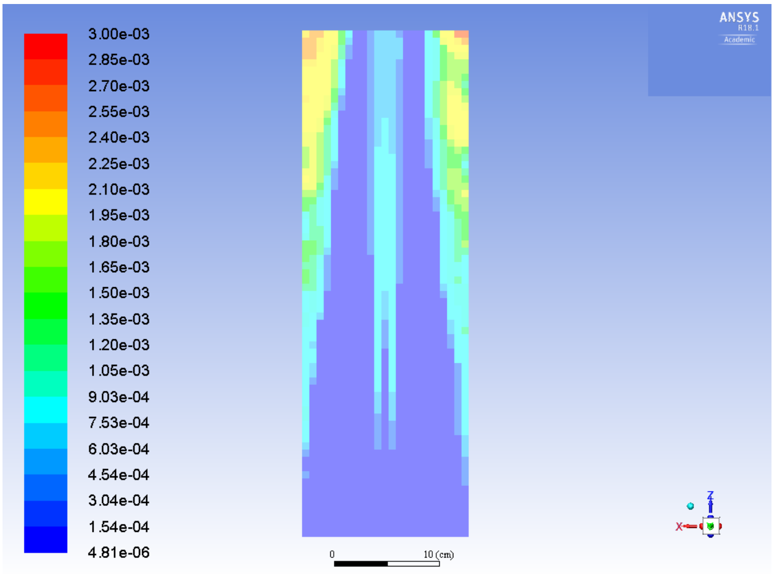

Figure 4.14: A cross section of the $\mathrm{Re} = 2000$ jet containing the jet center axis, displaying the turbulent viscosity from the Fluent solution for the $23 \times 23 \times 70$ RANS mesh. The scale is in units kg/m s. Boundary effects are visible along the edges.

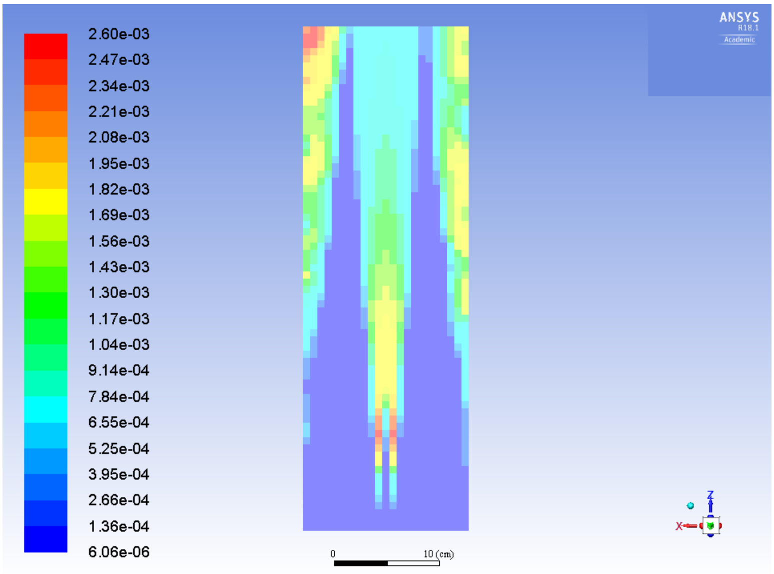

Figure 4.15: A cross section of the $\mathrm{Re} = 4000$ jet containing the jet center axis, displaying the turbulent viscosity from the Fluent solution for the $23 \times 23 \times 70$ RANS mesh. The scale is in units kg/m s. Boundary effects are visible along the edges.

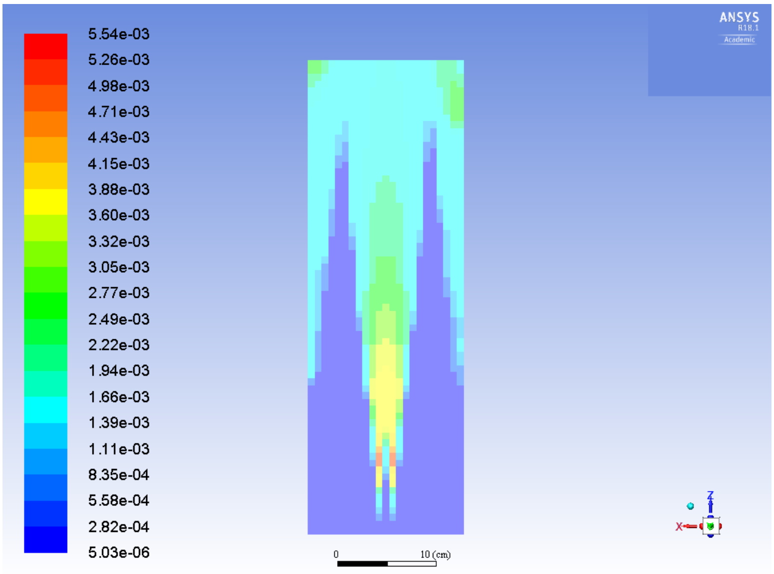

Figure 4.16: A cross section of the $\mathrm{Re} = 8000$ jet containing the jet center axis, displaying the turbulent viscosity from the Fluent solution for the $23 \times 23 \times 70$ RANS mesh. The scale is in units kg/m s. Boundary effects are visible along the edges.

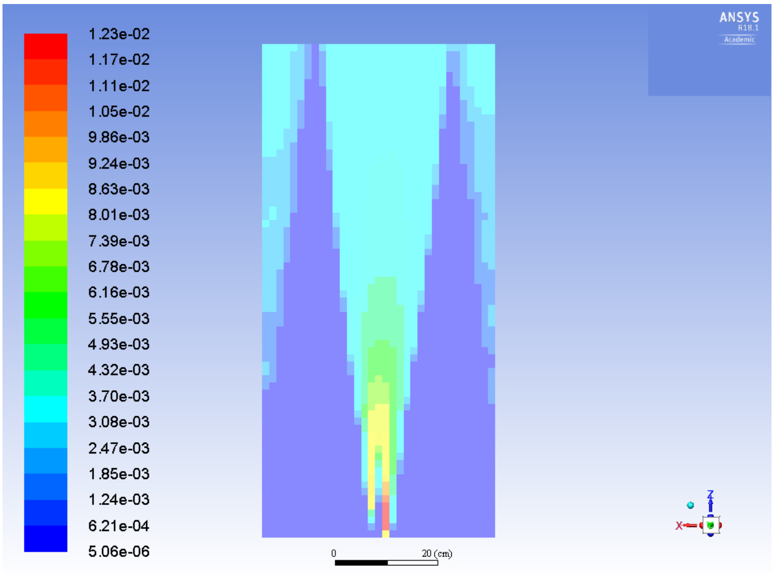

Figure 4.17: A cross section of the $\mathrm{Re} = 16000$ jet containing the jet center axis, displaying the turbulent viscosity from the Fluent solution for the $33 \times 33 \times 70$ RANS mesh. The scale is in units kg/m s. Boundary effects are visible along the edges.

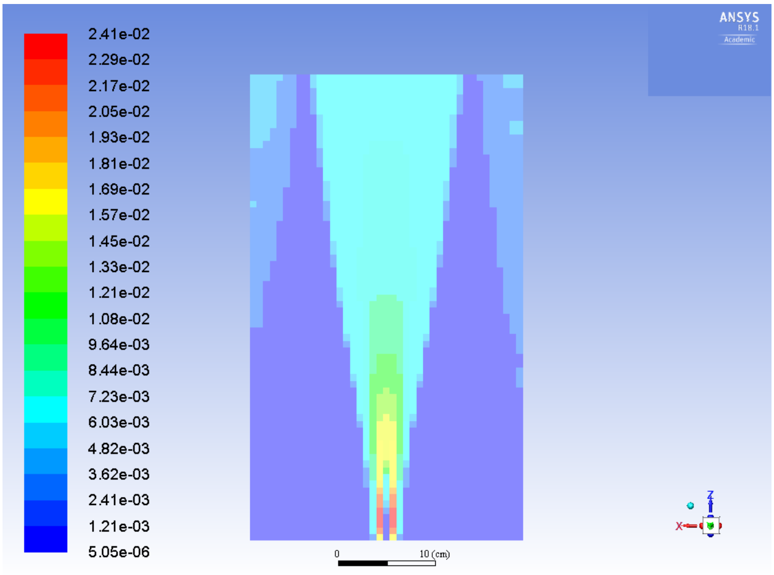

Figure 4.18: A cross section of the $\mathrm{Re} = 32000$ jet containing the jet center axis, displaying the turbulent viscosity from the Fluent solution for the $41 \times 41 \times 70$ RANS mesh. The scale is in units kg/m s. Boundary effects are visible along the edges.

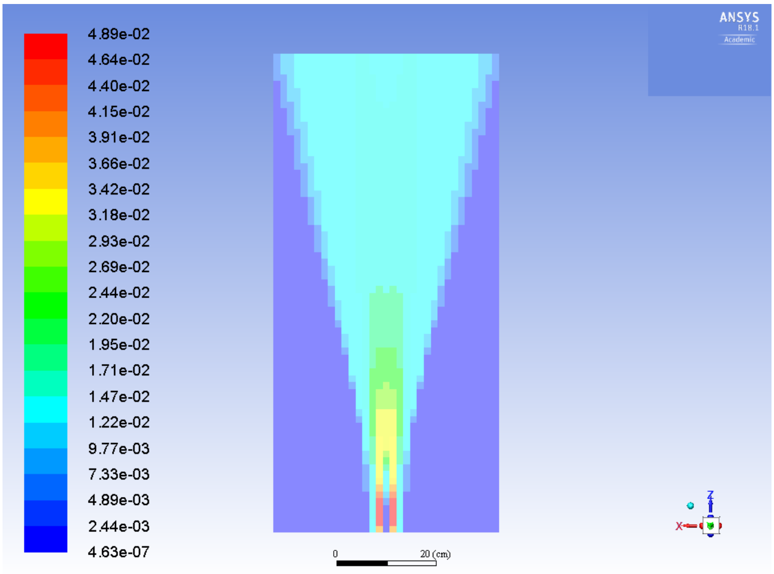

Figure 4.19: A cross section of the $\mathrm{Re} = 64000$ jet containing the jet center axis, displaying the turbulent viscosity from the Fluent solution for the $33 \times 33 \times 70$ RANS mesh. The scale is in units kg/m s.

4.2 Code Parallelisation and Performance

The effect of the code parallelisation was quite prominent. For a test case of a $23 \times 23 \times 38$ RANS mesh with a LEM resolution of 268 cells per 3DCV length, the running of the parallel code on four processors led to a run time reduction as large as 49.9%, which is a prominent improvement. This effectively reduced the run time from ~ 35.5 hours to ~ 18.5. For an equivalent run but with double LEM resolution, i.e. 538, the wall to wall run time is reduced by 43.8%, or a reduction from ~ 65.6 hours to ~ 36.9.

The scaling for larger number of threads the same scaling is approximately similar. Increasing for example 7 threads to 120 as in the most extreme case, ie. by a factor ~ 17, the run time was reduced by a factor close to 10.

For the CO_2/H_2-jet with Reynolds number 64000 a short LEM resolution refinement was performed, where LEM resolution vs. run time was investigated. The results are shown in Table 4.1, and all simulations were run on 6 threads (on hyper-threaded 4 core processors) using the exact same hardware. In the same table, the maximum relative error between a root-mean-squared differential diffusion solution and the next lower resolved solution are calculated, illustrating that the solution is not quite stable for LEM resolutions of this magnitude. A substantial resolution increase would be necessary to find perfectly stable solutions.

LEM resolution	Run time	Relative increase	Max. relative z_{rms} error
46	585m49.440s	-	-
68	1289m15.975s	120.3 %	-47.8 %
100	3246m48.718s	151.8 %	-44.0 %

Table 4.1: The run times for the CO_2/H_2 Jet at different LEM resolutions along with the relative increase for the previous LEM resolution in run time. The LEM resolution is given as the number of LEM wafers per 3DCV length. The maximum relative error between the current z_{rms} solution and the previous one is also presented.

For the same case as in the previous paragraph, a run with LEM resolution 46 was performed for 4 and 6 threads to examine the impact on run time while utilising hyper-threading. A time reduction of 13.2% was found, showing that increasing the number of parallel processes beyond the number of cores only has minor, yet positive effects on code performance for the limited number of threads used.

4.3 Differential Diffusion in LEM3D

4.3.1 The H_2/Freon 22 Jet

The differential diffusion in the hydrogen-freon jet was calculated for the radial direction at jet axis positions $x/D_j = 10, 20$, and 30 based on a $23 \times 23 \times 38$ RANS solution with LEM resolutions 128, 256, and 512. The jet Reynolds number was set to $\mathrm{Re} = 20000$, corresponding to a inlet velocity $U_{\mathrm{jet}} = 73$ m/s. The root-mean-squared differential diffusion as defined by Eq. (2.7) is given in Figures 4.20, 4.21, and 4.22. The similar quantities for a $69 \times 69 \times 114$ RANS solution are presented in Figures 4.23, and 4.24. Finally, the input data from the fine mesh adapted to a coarse grid generates results as in Figure 4.25, and 4.26.

4.3.2 The CO_2/H_2 Jet in Air Co-flow

Simulations resulted in data on both radial mean and root-mean-square differential diffusion values for the 64% CO_2 and 36% H_2 jet. The jet in this case was placed in a 1.5 m/s air co-flow. Simulations were performed for $\mathrm{Re} = 2000, 4000, 8000, 16000, 32000$, and 64000. Mean differential diffusion data for the two lowest Reynolds numbers are shown in Figures 4.27 and 4.28, along with LES results for comparison. The mean diffusion is here defined as $z = \xi_{H_2} - \xi_{CO_2}$. In Figures 4.29 and 4.30 the root mean squared differential diffusion is presented as a function of Reynolds numbers for different positions in the jet. Experimental data measured using Raman scattering spectroscopy by Smith et al. [2] is also given in the two figures. Root-mean-squared data for the entire sequence of Reynolds numbers are displayed in Figures 4.31, 4.32, 4.33, 4.34, 4.35, and 4.36. The profiles are given at the following set of positions $x/D_j = 15, 30$, and 60.

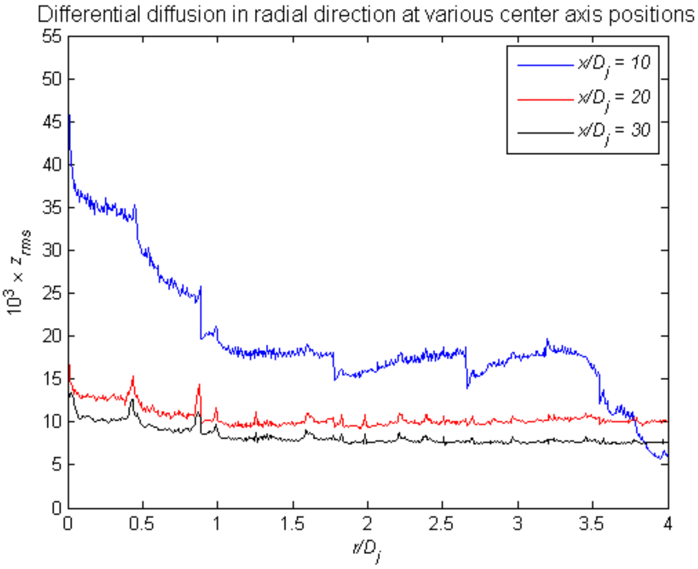

Figure 4.20: The radial root-mean-square profile for differential diffusion at different jet center axis positions, x. All length parameters are scaled by the jet diameter $D_j = 0.53$ cm. The data is based on the coarsest 23 × 23 × 38 RANS mesh with RANSdx = 0.4697 cm, and LEMres = 128.

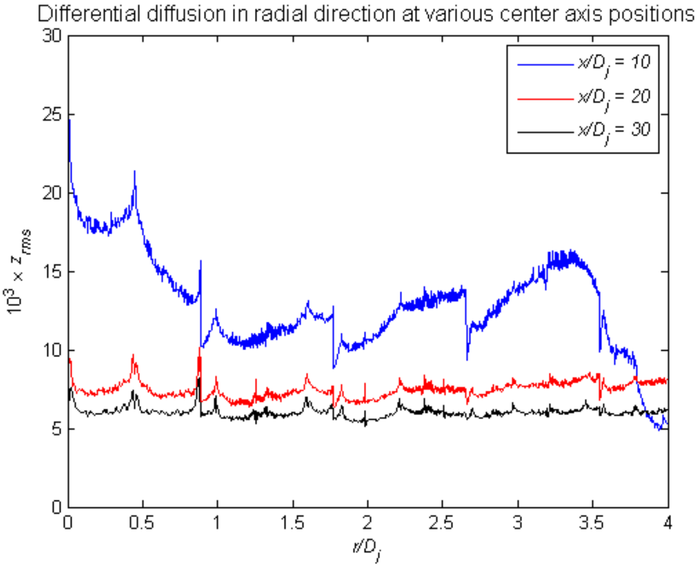

Figure 4.21: The radial root-mean-square profile for differential diffusion at different jet center axis positions, x. All length parameters are scaled by the jet diameter $D_j = 0.53$ cm. The data is based on the coarsest 23 × 23 × 38 RANS mesh with RANSdx = 0.4697 cm, and LEMres = 256.

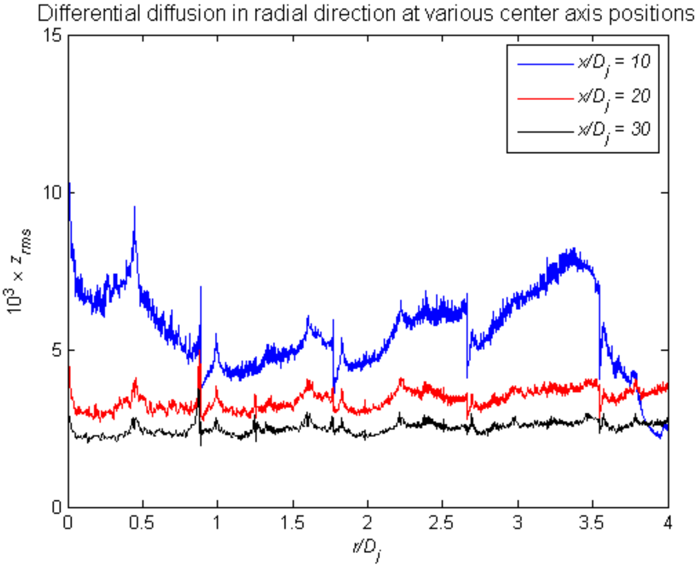

Figure 4.22: The radial root-mean-square profile for differential diffusion at different jet center axis positions, x. All length parameters are scaled by the jet diameter $D_j = 0.53$ cm. The data is based on the coarsest $23 \times 23 \times 38$ RANS mesh with RANSdx = 0.4697 cm, and LEMres = 512.

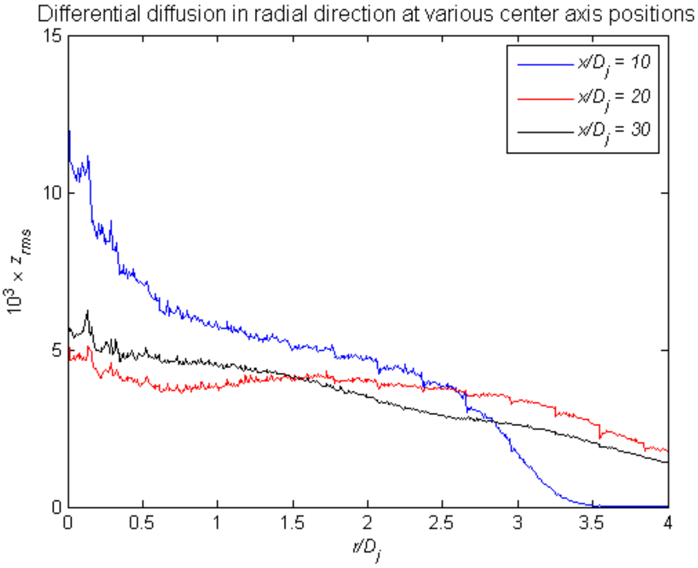

Figure 4.23: The radial root-mean-square profile for differential diffusion at different jet center axis positions, x. All length parameters are scaled by the jet diameter $D_j = 0.53$ cm. The data is based on the finest $69 \times 69 \times 114$ RANS mesh with RANSdx = 0.1566 cm, and LEMres = 42.

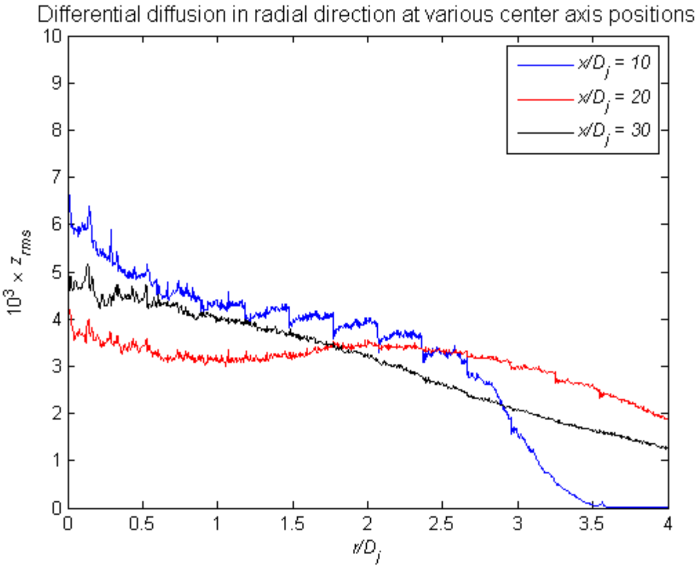

Figure 4.24: The radial root-mean-square profile for differential diffusion at different jet center axis positions, x. All length parameters are scaled by the jet diameter $D_j = 0.53$ cm. The data is based on the finest 69 × 69 × 114 RANS mesh with RANSdx = 0.1566 cm, and LEMres = 84.

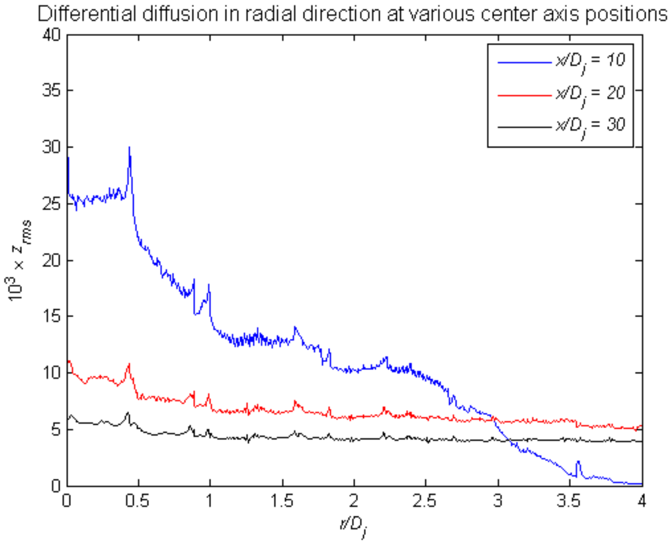

Figure 4.25: The radial root-mean-square profile for differential diffusion at different jet center axis positions, x. All length parameters are scaled by the jet diameter $D_j = 0.53$ cm. The data is based on the finest mesh solution modified to fit a 23 × 23 × 38 RANS mesh with RANSdx = 0.4697 cm, and LEMres = 128.

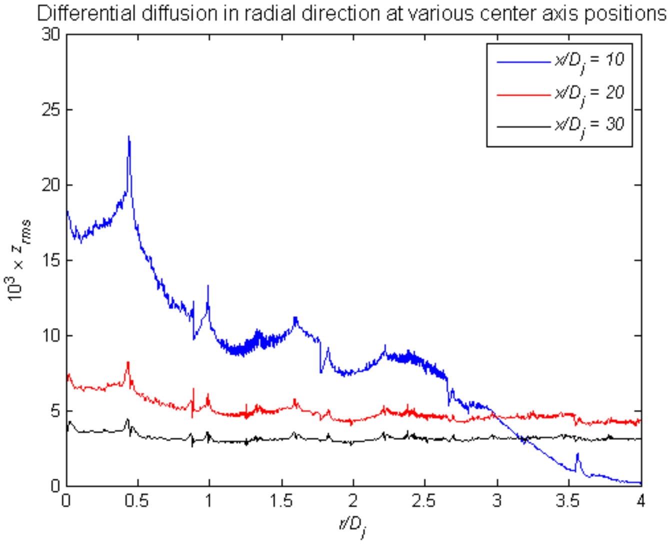

Figure 4.26: The radial root-mean-square profile for differential diffusion at different jet center axis positions, x. All length parameters are scaled by the jet diameter $D_j = 0.53$ cm. The data is based on the finest mesh solution modified to fit a $23 \times 23 \times 38$ RANS mesh with RANSdx = 0.4697 cm, and LEMres = 256.

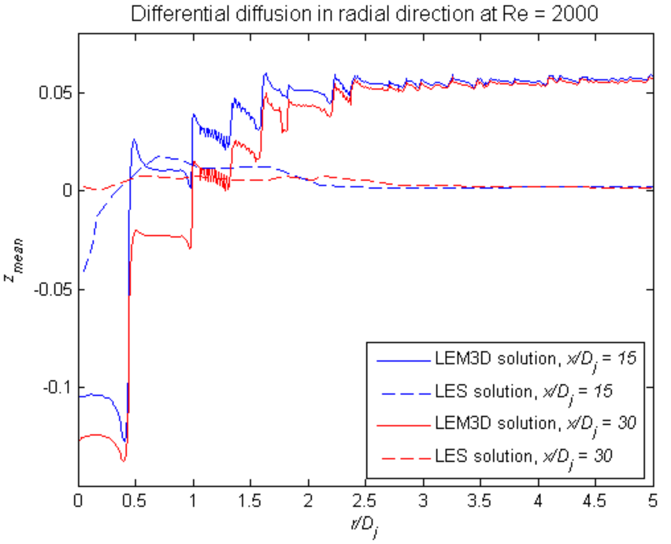

Figure 4.27: The radial profile for the mean differential diffusion at different jet center axis positions, x. The data is plotted together with LES results by Maragkos et al. [3]. All length parameters are scaled by the jet diameter $D_j = 0.77$ cm. The data is based on a $23 \times 23 \times 70$ RANS mesh with RANSdx = 0.6824 cm, and LEMres = 90. The CO_2/H_2 jet has Reynolds number 2000.

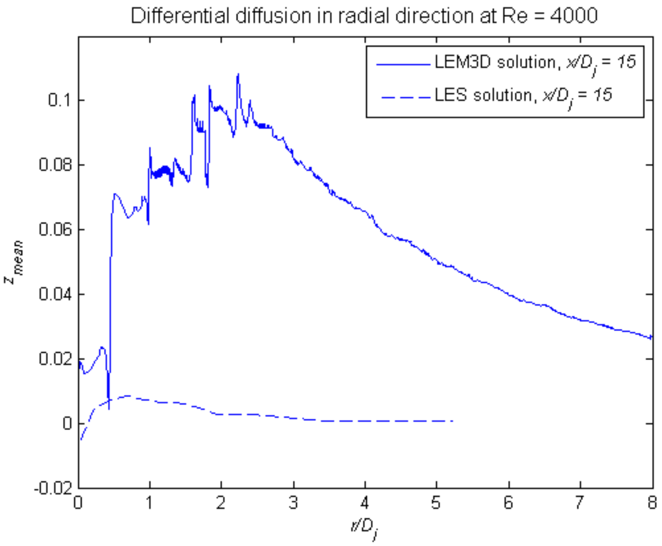

Figure 4.28: The radial profile for the mean differential diffusion at jet center axis position, $x/D_j = 15$. The data is plotted together with LES results by Maragkos et al. [3]. All length parameters are scaled by the jet diameter $D_j = 0.77$ cm. The data is based on a $23 \times 23 \times 70$ RANS mesh with RANSdx = 0.6824 cm, and LEMres = 100. The CO_2/H_2 jet has Reynolds number 4000.

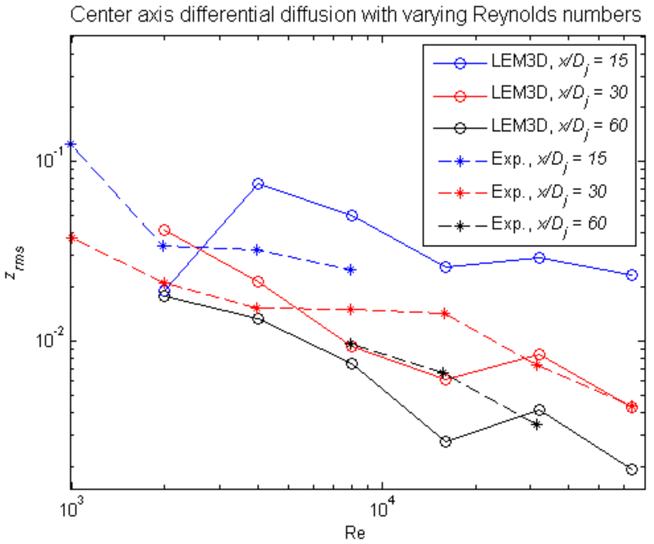

Figure 4.29: The root-mean-square values for differential diffusion at different Reynolds numbers and jet center axis positions, x. Experimental values for an identical CO_2/H_2 jet measured by Smith et al. [2] are also given. All length parameters are scaled by the jet diameter $D_j = 0.77$ cm.

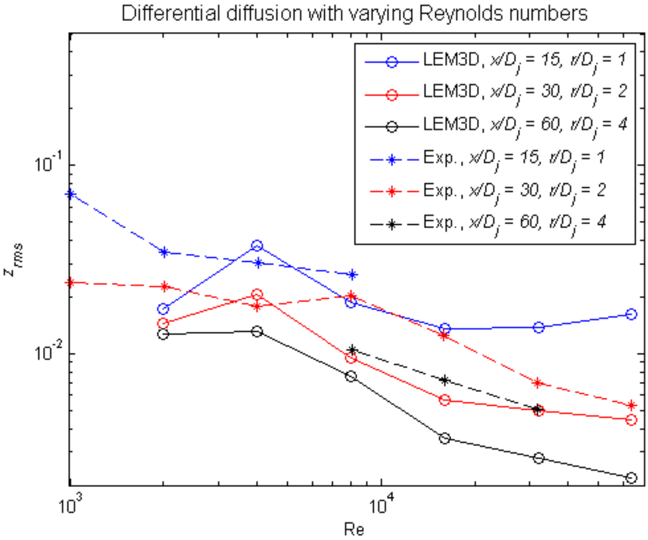

Figure 4.30: The root-mean-square values for differential diffusion at different Reynolds numbers, jet center axis positions x, and radial offsets r. Experimental values for an identical CO_2/H_2 jet measured by Smith et al. [2] are also given. All length parameters are scaled by the jet diameter $D_j = 0.77$ cm.

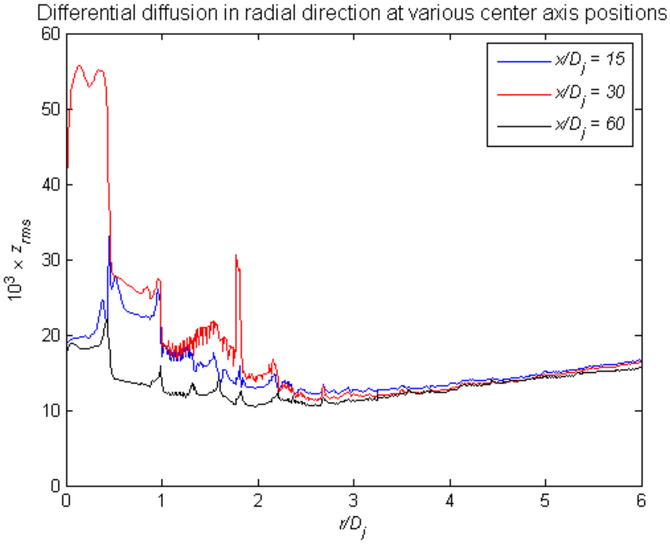

Figure 4.31: The radial root-mean-square profile for differential diffusion at different jet center axis positions, x. All length parameters are scaled by the jet diameter $D_j = 0.77$ cm. The data is based on a $23 \times 23 \times 70$ RANS mesh with RANSdx = 0.6824 cm, and LEMres = 90. The CO_2/H_2 jet has Reynolds number 2000.

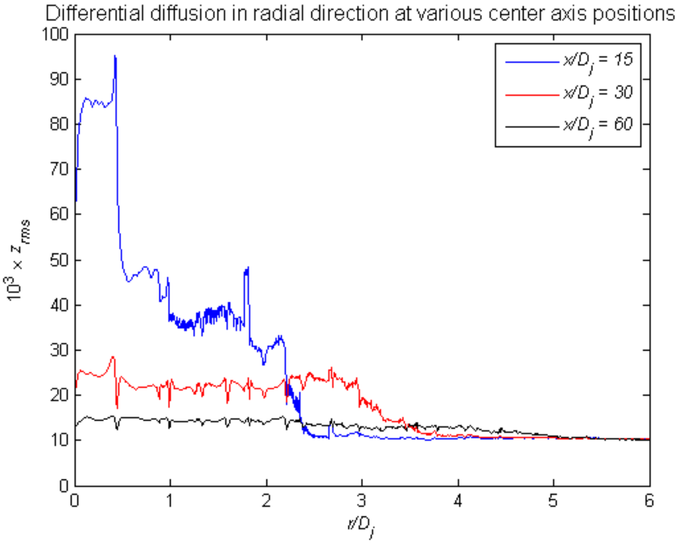

Figure 4.32: The radial root-mean-square profile for differential diffusion at different jet center axis positions, x. All length parameters are scaled by the jet diameter $D_j = 0.77$ cm. The data is based on a $23 \times 23 \times 70$ RANS mesh with RANSdx = 0.6824 cm, and LEMres = 140. The CO_2/H_2 jet has Reynolds number 4000.

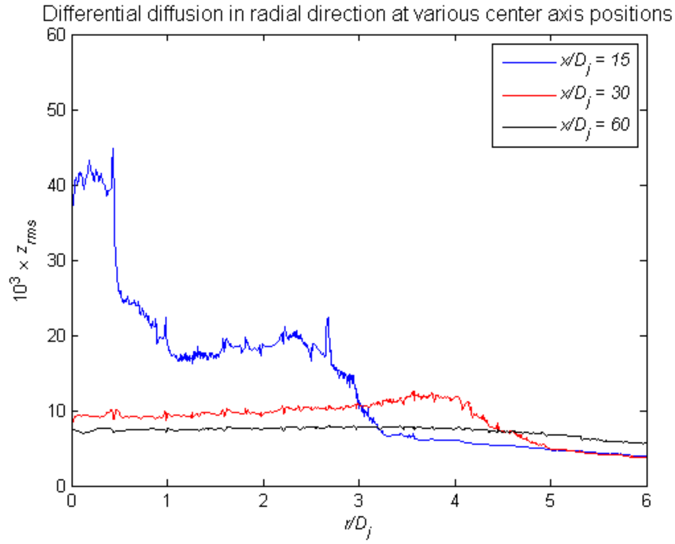

Figure 4.33: The radial root-mean-square profile for differential diffusion at different jet center axis positions, x. All length parameters are scaled by the jet diameter $D_j = 0.77$ cm. The data is based on a $23 \times 23 \times 70$ RANS mesh with RANSdx = 0.6824 cm, and LEMres = 140. The CO_2/H_2 jet has Reynolds number 8000.

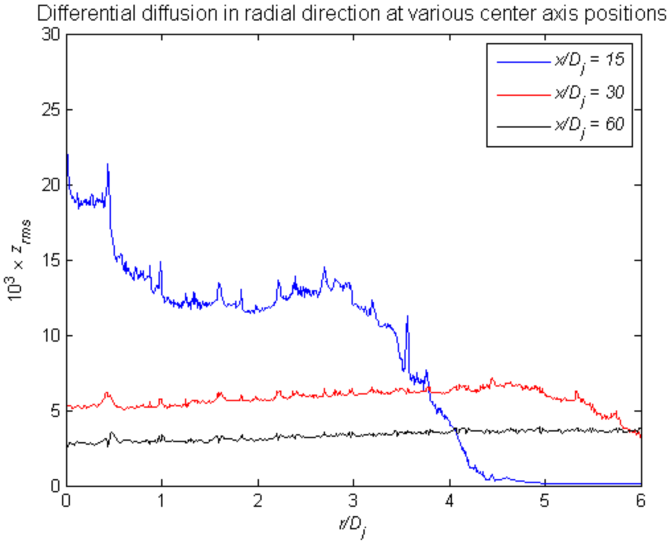

Figure 4.34: The radial root-mean-square profile for differential diffusion at different jet center axis positions, x. All length parameters are scaled by the jet diameter $D_j = 0.77$ cm. The data is based on a $33 \times 33 \times 70$ RANS mesh with RANSdx = 0.6824 cm, and LEMres = 100. The CO_2/H_2 jet has Reynolds number 16000.

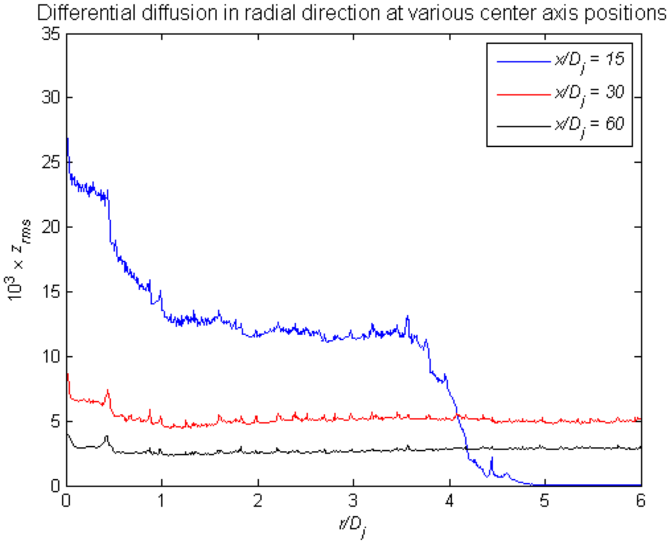

Figure 4.35: The radial root-mean-square profile for differential diffusion at different jet center axis positions, x. All length parameters are scaled by the jet diameter $D_j = 0.77$ cm. The data is based on a $41 \times 41 \times 70$ RANS mesh with RANSdx = 0.6824 cm, and LEMres = 100. The CO_2/H_2 jet has Reynolds number 32000.

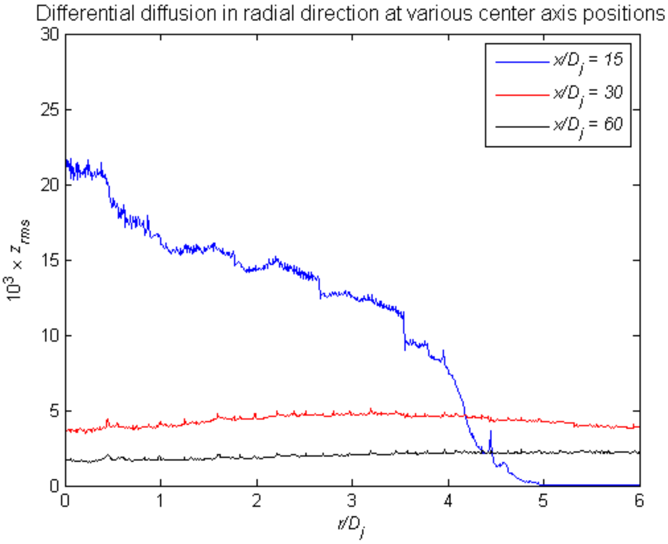

Figure 4.36: The radial root-mean-square profile for differential diffusion at different jet center axis positions, x. All length parameters are scaled by the jet diameter $D_j = 0.77$ cm. The data is based on a $33 \times 33 \times 70$ RANS mesh with RANSdx = 0.6824 cm, and LEMres = 100. The CO_2/H_2 jet has Reynolds number 64000.

Chapter 5

Discussion

5.1 RANS Solutions

First the RANS solutions for the H_2/Freon 22 jet are examined. As seen in Figures 4.5, 4.6 and 4.7, there are some distinct differences in the fine, modified and coarse mesh outputs. The streamwise u-velocity of the coarse solution consistently lies above the fine mesh, and similarly for the turbulent viscosity, but the magnitude of the deviations are seen clearly in Figures 5.1 and 5.2. It is apparent that the fine and modified solutions are very similar, except for at the immediate inlet situations. There are bigger differences between the course and fine mesh. Both the molecular viscosity, the turbulent viscosity and the streamwise velocity are generally larger for the coarsest mesh, which explains why for example the run times, were observed to be quite a lot higher for the fine, and modified meshes. This will be discussed in more detail later. The high turbulent diffusivity for the coarsest mesh, which has a maximum relative difference to the fine mesh of nearly 200% will have effects on the resolution of turbulent scales.

The carbon dioxide-hydrogen jet suffered from some edge effects along the boundaries, and toward the downstream end of the flow, which is apparent from all Figures 4.14 through 4.19. That is the reason for why the width and height of the jets were gradually increased as the jet width increased for higher Reynolds numbers. As explained in Section 3.2, the edge effects were removed by using a UDF cleaning the output file. The UDF uses gradients and multiple sweeps to smooth the profile, which means that in cases where the edge effect overlaps with the actual solution, the solution may not be very precise in relation to the true solution, but is realistic in that the profile is smoothed out. In the low Reynolds number Figures 4.8 and 4.9, it is apparent that the co-flow is nearly indistinct from the jet flow, and this may have some implications for mixing outside of the jet itself.

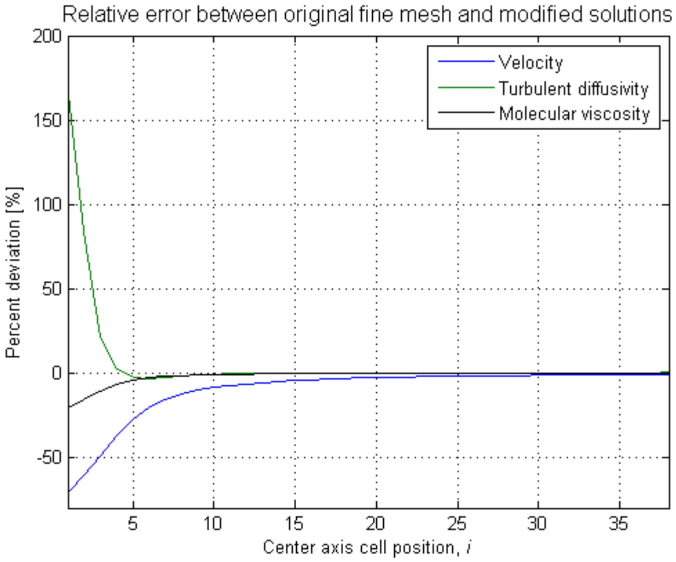

Figure 5.1: The streamwise u-velocities, turbulent diffusivities and molecular viscosities of the finest refined mesh, compared to the modified solution adapted to a 23 × 23 × 38 RANS mesh.

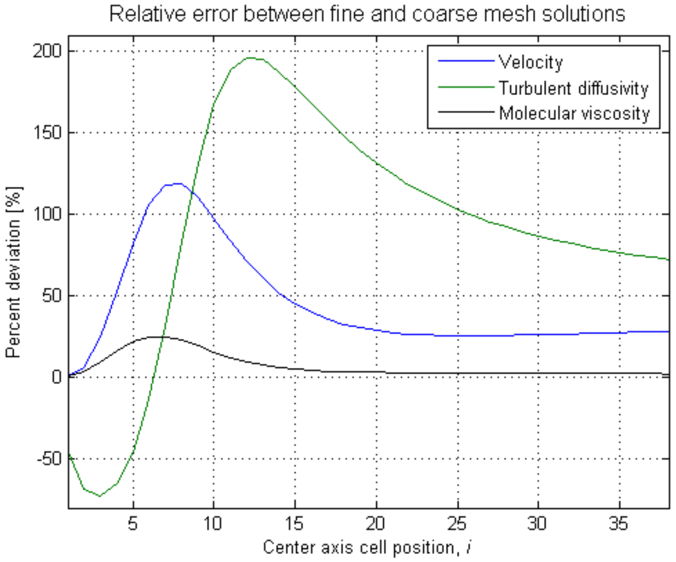

Figure 5.2: The streamwise u-velocities, turbulent diffusivities and molecular viscosities of the finest refined mesh, compared to the coarse 23 × 23 × 38 RANS mesh solution.

5.2 Differential Diffusion Results for LEM3D

5.2.1 The H_2/Freon 22 Jet

The results for the H_2/Freon 22 jet to some extent reproduce the behaviour observed by Sannan et al. [16]. Falling magnitude with higher radial distance and with higher LEM resolution is observed, except that in this case, the 512 LEM resolved solution also falls quite low in general magnitude level and has a very slow descent with radial coordinates. Considering the coarsest RANS mesh, this is especially apparent at $x/D_j = 10$, and the results by Sannan et al. do not share the same peak at $x/D_j \sim 3.3$. Otherwise, the differential diffusion decreases with increased distance from the jet inlet, which is according to expectations. For LEMres = 128 and 256 the differential diffusion is far higher near the center axis than the rest of the jet. This may indicate that the peak near the end of the $x/D_j = 10$ profile is an important profile feature, which will not be subdued by the falling profile magnitude. For the profile with LEMres = 512, the lkfac is set as low as 2, which effectively allows more small eddies to appear, and their effect may explain why less matter diffuses out from volumes close to the jet center axis than for coarser resolutions. In addition, by defining the edge of the jet at $0.01 \times U_{\max}$, i.e., at one percent the magnitude of the maximum mean u-velocity component, the edge of the jet at $x/D_j = 10$ can be estimated to be $\delta_{\text{edge}} = 3.928$ cm from the jet center axis. The edge coincides well with where the differential diffusion decays and approaches zero.

The fine RANS mesh, gives a much smoother solution. Figures 4.23 and 4.24 illustrate that the general trend where the differential diffusion decreases for increasing streamwise and radial coordinates. The same trend is observed for increasing LEM resolution as well. It is interesting to note that the differential diffusion is higher for the profile at $x/D_j = 30$ than for $x/D_j = 20$ for small r. Another feature that separates this solution from the coarse RANS solution is the high, constant negative gradient for the $x/D_j = 30$ solution which implies a more complex differential diffusion behaviour downstream than what the coarse RANS mesh allows for. Using the finely resolved RANS solution, the jet width at $x/D_j = 10$ is estimated to $\delta_{\text{edge}} = 2.945$ cm, which again coincides well with the decay of the LEM3D solution.

Finally, the modified solution is considered as represented in Figures 4.25 and 4.26. The downstream, radial and LEMres variation is more consistent with the coarse RANS case than the finest. However, it still obeys the jet width of the fine RANS input.

In common for all resolutions is that the LEM3D predicts high differential diffusion near the center axis, and decreasing yet almost uniform differential diffusion until the full width of the jet is reached. Further downstream the differential diffusion seems to become steadily more uniform within the confines for the jet. The slightly deviating behaviour from the finest RANS mesh case is likely due to the much improved resolution of the turbulent properties and mean velocity field of the jet. The Kolmogorov scale should be sufficiently resolved, so all turbulent behaviour should be captured. This is discussed in closer detail in Section 5.4. Also, since the coarse and modified mesh solutions are both based on $23 \times 23 \times 38$ meshes, it is likely that the distinct fine mesh profile is a consequence of the finer RANS resolution.

The LEM3D is readily compared to experimental data in Figures 5.3, 5.4, and 5.5. Dibble et al. [1] produced the experimental values by use of Rayleigh scattering. The comparison reveals two very distinct differences, the first being that the computational results have a much lower magnitude, which means the simulations roughly underestimate the experimental results by a factor between 1.1 and 10. Considering the coarse RANS configuration in Figure 5.3, the profiles at $x/D_j = 10$, and 20 fit quite well with the radial extent and decaying behaviour of the experimental data. The same is true for the modified RANS configuration, which also matches even better in terms of magnitude. It must also be noted that for the experimental data the furthest upstream profile seems to level off at a value of $r/D_j \sim 5$ after a sharp decline at the edge of the jet. This lies in the area that should be outside the jet, and which would normally experience negligible differential diffusion. Therefore, it may be assumed that the experimental data has a maximum uncertainty of ± 5 units. That would explain some of the underestimation of the LEM, but cannot account for all of it. In comparison, the two profiles that are furthest downstream and based on the fine RANS mesh input, decay to zero far earlier than the experimental data. The profiles therefore indicate a narrower jet than in the experiment, or that no mixing action is performed in the extremities of the jet. This solution is better however, at reproducing the wide peak which the middle distance profile experiences for $x/D_j \sim 3.5$. The low magnitude, also indicates that the true stationary solution which the LEM3D seeks, is yet to be reached through even higher refinement.

The second major difference is that the experimental data for the $x/D_j = 10$ profile has a large peak at $r/D_j = 2$. Only the modified RANS solution input has a peak which weakly resembles this, but it is a better fit with the experimental profile than the other two. It is also interesting to note that in Figure 5.5, the the radial positions where the $x/D_j = 10$ intersect the other two profile matches experimental data very well. The same is also true for the intersection between the $x/D_j = 20$ and 30 profiles. An even finer refined RANS mesh, for example $207 \times 207 \times 342$ modified to fit the $69 \times 69 \times 114$ or $23 \times 23 \times 38$ mesh, would give even more precise velocity and turbulence property profiles which likely would benefit even more from the modification.

In general the LEM3D predicts high differential diffusion close to the jet center axis, and almost uniform diffusion until the edge of the jet is reached. Differential diffusion is here defined as the difference between the hydrogen and Freon 22 mixing fractions which means that the highest values are where there is a large difference between the transport of the more diffusive species (hydrogen) than for the less diffusive species. Hence this indicates that LEM3D predicts hydrogen to diffuse from the jet center upstream, and that the diffusion and mixing is more uniform downstream and further out radially. This is realistic as air is entrained in the early development of the jet, and would possibly affect the hydrogen diffusion far upstream.

The effects of further refinement for the different mesh configurations are expected to further decrease the magnitude of the diffusion, and diminish the high values near the center axis compared to the rest of the jet domain, at least this is what the current observed trends suggest.

It was discovered after the LEM3D simulations were performed that the Fluent output for the finest mesh had irregularities in the inlet boundary condition. Not all of the 9 inlet cells had an effective inlet velocity of 73 m/s, and the velocity was asymmetrically distributed as a result. The effect would be a reduced Reynolds number, and that the modified mesh solution would get a more imprecise velocity profile with respect to the inlet boundary condition. In Figures 5.6 and 5.7 the corrected profiles are shown. Here, the finely resolved Fluent solution has been subjected to stricter conditions on the inlet boundary conditions. It is evident from the velocity profiles that the fine and coarse solutions are now in better agreement. The modified solution velocity does now fulfil the boundary condition, but otherwise has a similar profile as before the error correction. The effect of the error would lessen the mass inflow, and otherwise affect the inlet velocity field for the modified solution, but is expected not to change downstream radial profiles in the steady state to a large degree. As will be discussed in subsection 5.2.2, higher Reynolds numbers are known to decrease the differential diffusion, which means that the inlet error should cause small increases in the differential diffusion profiles.

Another source of error should be that the boundary condition is not well adapted to a 3×3 inlet in the LEM3D code. The result should most likely not suffer greatly from this, but should be improved for future repetitions of similar flow configurations. A possible effect is that it may contribute to the quick decay to zero for the downstream radial profiles. Despite the errors just described, the computed profiles are expected to display the characteristic behaviour for each of the seven solutions. Some of the differential diffusion magnitudes are, however, inaccurate due to the input errors, but as has been observed, the LEMres dependency probably has a much stronger effect on the magnitudes. However, for future simulations the corrected input and boundary condition should of course be utilised.

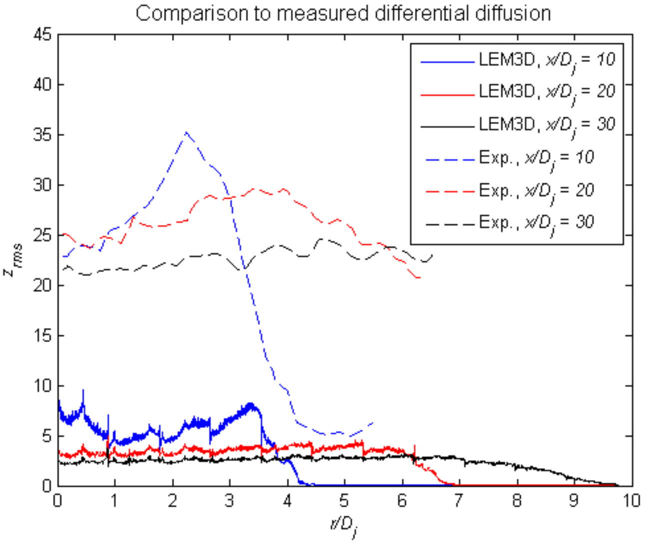

Figure 5.3: The radial root-mean-square profile for differential diffusion at multiple jet center axis positions, x. Experimental data by Dibble et al. [1] is presented for comparison. All length parameters are scaled by the jet diameter $D_j = 0.53$ cm. The LEM3D data is based on the coarsest resolved $23 \times 23 \times 38$ RANS mesh with RANSdx = 0.4697 cm, and LEMres = 512.

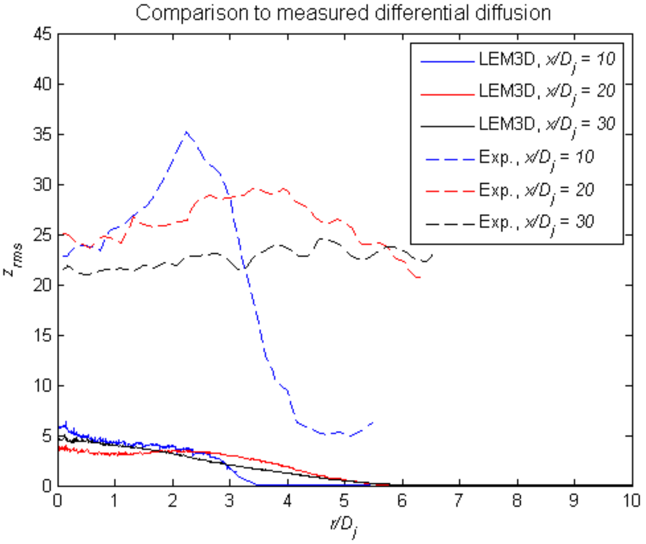

Figure 5.4: The radial root-mean-square profile for differential diffusion at multiple jet center axis positions, x. Experimental data by Dibble et al. [1] is presented for comparison. All length parameters are scaled by the jet diameter $D_j = 0.53$ cm. The LEM3D data is based on the finest resolved $69 \times 69 \times 114$ RANS mesh with RANSdx = 0.1566 cm, and LEMres = 84.

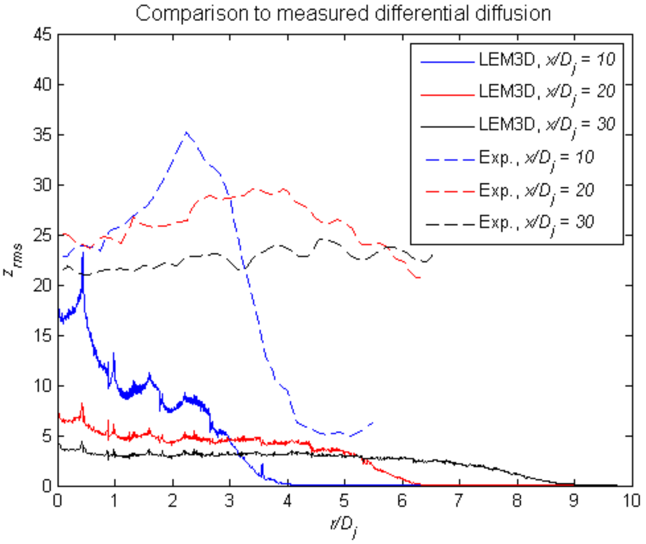

Figure 5.5: The radial root-mean-square profile for differential diffusion at multiple jet center axis positions, x. Experimental data by Dibble et al. [1] is presented for comparison. All length parameters are scaled by the jet diameter $D_j = 0.53$ cm. The LEM3D data is based on the finest mesh solution modified to fit a 23 × 23 × 38 RANS mesh with RANSdx = 0.4697 cm, and LEMres = 256.

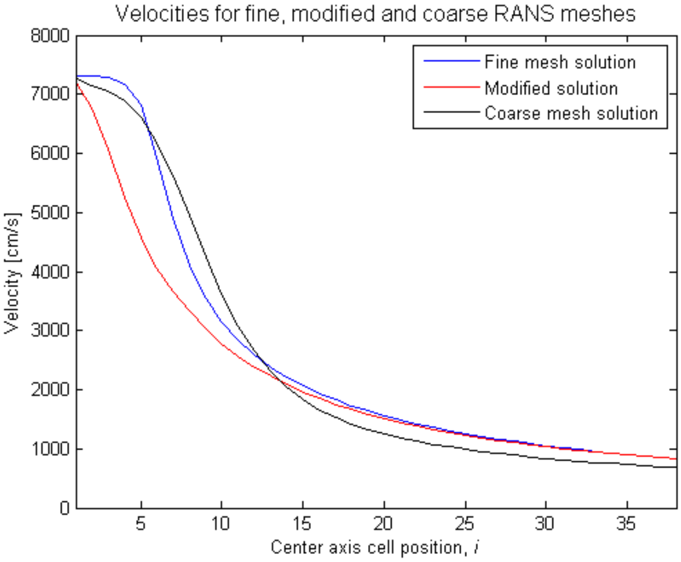

Figure 5.6: The stream wise u-velocities of the finest refined mesh along the jet center axis, compared to the modified solution adapted to a 23 × 23 × 38 RANS mesh, and the direct coarse mesh solution. For this data, the inlet boundary condition is better implemented than previously.

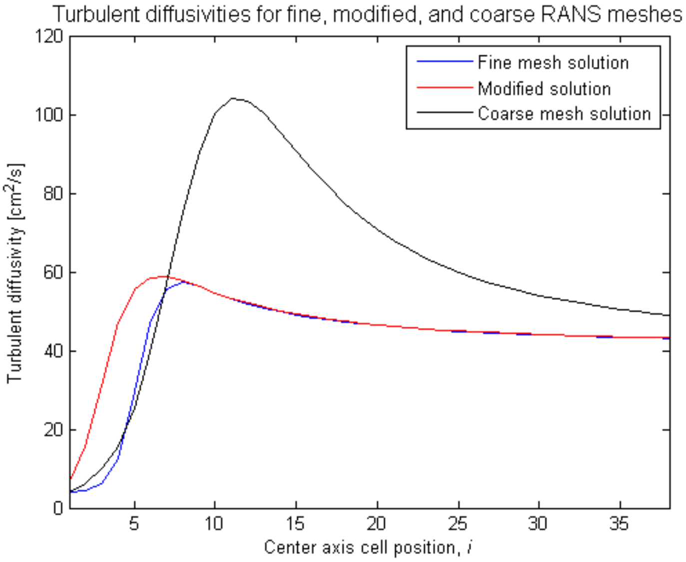

Figure 5.7: The turbulent diffusivities of the finest refined mesh, along the jet center axis, compared to the modified solution adapted to a $23 \times 23 \times 38$ RANS mesh, and the direct coarse mesh solution. For this data, the inlet boundary condition is better implemented than previously.

5.2.2 The CO_2/H_2 Jet

Figures 4.27 and 4.28, display the mean radial differential diffusion between hydrogen and carbon dioxide along with LES data by Maragkos et al. [3] for $\mathrm{Re} = 2000$ and 4000. For $\mathrm{Re} = 2000$ there is not an entirely decisive agreement between the experiments and simulations. Both sets of simulation data recognise a high differential diffusion close to the jet center axis, and then a segment of relaxation towards a stable level. Experimental data agrees for $x/D_j = 15$, with a relaxation towards zero, but the profile further downstream has low diffusion near the jet center axis. The LEM3D mean overestimates the experimental data by over two orders of magnitude in the most extreme points. The $\mathrm{Re} = 4000$ case has an opposite trend, where both experiment and simulation agree that less differential diffusion happens by the central axis than immediately outside, and the peak decays slowly towards zero. In general, the profiles show similar behaviour as experiments, but also large overestimation of experimental data.

Figures 4.29 and 4.30 show experimental data by Smith et al. [2], and the rms LEM3D solutions as functions of Reynolds numbers, for different locations within the jet. The first figure displays data along the jet center axis and reveals general very good agreement with the experiments. The $x/D_j = 10$ profile is somewhat overestimated, while the $x/D_j = 30$ profile is underestimated. The second figure also shows good agreement with the general trend of the three profiles, but in this case LEM3D underestimates the experimental data by sometimes a factor close to three. For both figures though, there is some strange behaviour in the $\mathrm{Re} = 2000$ values. For the first figure, the differential diffusion of the furthest upstream profile is smaller than the next downstream profile, which is contrary to the general trend, and also these values are quite low for the second figure. A possible explanation may be that the profiles produced by LEM are quite jagged, and may at some points be slightly over or underestimated, and in addition the $\mathrm{Re} = 2000$ results are more poorly resolved than the others which may have a slight effect. The two plots confirm that LEM3D predicts the effects of differential diffusion to decrease with higher Reynolds numbers, and that this agrees well with experimental measurements.

Figures 4.31 through 4.36 show the radial differential diffusion profiles for the different Reynolds numbers. The LEM3D solutions highlight high differential diffusion close to the center axis, and an almost uniform level of diffusion throughout the rest of the jet width. The width of the mixing region is shown to widen with higher Reynolds numbers. It is also apparent that the co-flow has a noticeable effect in the low Reynolds number results. For Reynolds numbers 2000 - 8000 it is seen that the co-flow ensures a minimum level of mixing for the area outside the jet as well as within it. In the most extreme case where the jet inlet velocity is only double that of the co-flow, which is for $\mathrm{Re} = 2000$, the LEM3D predicts increasing differential diffusion even outside the jet due to the co-flow interaction. For the subsequent figures, the co-flow effect steadily diminishes. A strange artefact observed in Figure 4.31, is that the differential diffusion in the middle position profile is higher than for the profile closest to the inlet, which is contrary to other trends. The jet should be sufficiently resolved, as discussed in more detail in Section 5.4, and therefore it is likely that this is an effect of the flow configuration, and since the distinction between jet and co-flow is so small it is likely an effect of the co-flow influence.

To conclude, the differential diffusion predicted for the CO_2/H_2 mixture by LEM3D is generally consistent with the results for the $H_2/CHClF_2$ jet. This is unsurprising since the molecular diffusivity of the two heavier species, CO_2 and Freon 22, are comparable, while hydrogen is highly diffusive. There are some noticeable differences, which are most likely due to co-flow influence, and the fact that the LEM wafer resolution is between half and three quarters of the coarsest LEM resolution used for the hydrogen-Freon 22 mixture.

5.3 Details on the Simulation Execution

The parallelisation of the code was very beneficial, since this greatly reduced run times in comparison to sequential code, as demonstrated in Section 4.2. Yet, the run time growth with resolution was still quite fast as seen in the same section, so computational demands were high. Run times for simulations with different RANS resolutions but equivalent LEM resolution were also wildly different, where the finest RANS mesh demanded the most computational time. The larger RANS meshes also required multiple arrays in the code to be enlarged 27 times, and caused high demands for RAM. A consequence of this was that not all of the nodes used for computations could satisfy the RAM demands, and therefore some simulations had to be delayed until suitable resources were made available. Access to a larger multi node system was eventually acquired, but many users and a crowded work queue made it unfeasible to further refine LEM resolution for the finest

RANS meshes further than what is presented in the current results section. This system could allocate a high number of nodes to the parallelisation and greatly reduce run time.

The LEM3D was through experience shown to be very sensitive to input files, especially to the integral scale, since lower integral scale values would lead to more small eddies and more triplet map events. This results in more computational work, and longer run times. McMurtry et al. [22] used leading order analysis to obtain the rate parameter

$$\zeta = \frac{54}{5}\frac{\nu Re_t}{\Lambda^3}\left(\frac{\Lambda}{\eta}\right)^{\frac{5}{3}}, \tag{5.1}$$

from the Equation (2.28). The resulting expression clearly states that higher values of Λ will give a lower rate of events, ζ.

This fact was observed in multiple ways, for example, using the uncleaned integral scale files, with many erroneously high integral scale values the run time was reasonable, but when changing to the cleaned integral scale, the run time was well over doubled. Similarly, the input data produced with the coarse and fine RANS meshes in Fluent are so different that the run time for LEMres = 256, increases from just over 5 days for the coarsest mesh, to a prediction of approximately 21 days for the finest $69 \times 69 \times 114$ mesh. This observation is even further strengthened when investigating the modified RANS mesh solution. Simulations based on this technique, as explained in the final paragraphs of Section 3.2.2, had a run time comparable to the raw $69 \times 69 \times 114$ mesh of approximately 21 days.

As shown in Section 4.2, the scaling from 7 to 120 processes gave improved performance and was comparable to the performance scaling of going from one to four processes. The original run time was over 80 days. Since 7 by 4^2 is 112 and $80/2^2 = 20$, the approximate relation that the computational time is halved for each time the number of processes is quadrupled seems realistic. However, this is not a very rigid computation and differences in computer architecture and CPUs also affect this to a large extent. It should be noted that since only a single node handles the communication with all the other nodes, the parallelisation performance should eventually reach a ceiling where there communication node starts to slow down the program. This ceiling number of nodes rises however as the LEM resolution rises, and it takes longer for each node to compute a solution, and the communication with the root node may happen in a larger interval of time. This is very visible if considering that 7 threads on a 4 core hyper-threaded processor, was increased to 120 threads running on 120 processors. The hyper-threaded 7 processes are equivalent to a small improvement on a pure 4 processor system, as implied in Section 4.2. Counting this as 4 threads, the number of threads are increased by a factor $30 \approx 2^{4.9}$, which means the amount of threads that work on the finite number of LEM domains are doubled almost 5 times and ideally should reduce run time by half each time. Therefore one would expect a run time reduction by a factor close to 30. Instead, the run time was reduced by a factor 10, which is quite good, but demonstrates that the sequential code executed by the root thread, and intercommunication between processors has a prominent effect. Distributing the root node tasks on more processors would likely improve scaling properties, if possible.

5.4 Resolution of Turbulent Scales

In terms of resolution, the limiting quantity for turbulent eddies is the LEM wafer thickness lemdx, which must be at least a third of the eddy length in order for the eddy to be resolved, due to the definition of triplet maps.

The LEM resolution for the H_2/Freon 22 jet is varied as well as its RANS input resolution, and as such the resolution of Kolmogorov scale eddies differ for all cases. Due to the lkfac being set to a value higher than 1, the actual Kolmogorov scale was not actually resolved in all cases, but for many cases it would have been possible with the given resolution at cost of longer computational times. The Kolmogorov scale is computed locally, i.e., within the turbulent jet the turbulent structure is not uniform for the entire domain and therefore the Kolmogorov scale varies between each 3DCV. For the coarsest resolved RANS input data, the Kolmogorov scale would be resolved 4 - 22 times for the entire jet centerline. For the finest mesh, the smallest scale turbulence should also be sufficiently resolved, and it is resolved between 4 and 28 times along the center axis. It should be noted that the highest values are at the very end of the domain and may be partially caused by edge effects, but the general trend is that the resolution improves further downstream.

For the modified RANS mesh data, the resolution is again improved, with the Kolmogorov scale being resolved 3 - 28 times. The Kolmogorov resolution is constant for all the chosen LEMres values, since the lkfac is halved each time LEMres is doubled, and they therefore cancel out perfectly, which then allows the effect of higher LEM resolution to be investigated without changing the Kolmogorov resolution and saving computational time. From observations, the integral scales Λ typically are smaller for the finest mesh, and it would be expected that the Kolmogorov scale would be smaller and more poorly resolved for the finest mesh. The LEMres and 3DCV sizes are chosen such that the grid resolution for the LEMres = 128 and 256 solutions should be roughly equivalent to the fine RANS solution with LEMres = 42 and 84 respectively. From Figure 5.2 it is apparent that the coarsely resolved turbulent diffusivities have higher magnitudes, and since the code computes the Kolmogorov scale resolution by the equation

$$\eta = \frac{\Lambda}{e^{\frac{3}{4}\ln\frac{D_{\mathrm{T}}\mathrm{PrT}}{3\nu}}} = \Lambda\Big(\frac{D_{\mathrm{T}}\mathrm{PrT}}{3\nu}\Big)^{-\frac{3}{4}},$$

it explains why the Kolmogorov resolution still agrees so well for both solutions. It is then also important to note that the integral scale Λ is slightly lower for the finest RANS solution.

For the CO_2/H_2 jet, the resolution had to be limited with respect to run time restrictions. As observed in Section 4.2, the run time scales almost quadratically as $\sim w^2$, if w denotes the ratio between the new and old LEM resolutions. A level of LEMres = 100 was decided to be a suitable compromise for run time and resolution in general, and corresponds to a LEM wafer thickness of $6.824 \cdot 10^{-5}$ m. This turned out to be only suitable for the highest resolutions, as the lowest Reynolds number jet ($\mathrm{Re} = 2000$), experienced an extremely long run time compared to the others, and then resolution was decreased to

90, and heavier computational resources were needed. For $\mathrm{Re} = 4000, 8000$, the solutions suffered oscillations, and very sharp jumps until the resolution was increased until 140, or a wafer thickness of $4.874 \cdot 10^{-5}$ m. At this point it would probably be better to run a more thorough sensitivity analysis for the entire spectrum of Reynolds numbers, but as shown in Section 4.2, this would probably be unfeasibly time consuming, as the most powerful available computational resource was subject to a crowded work queue. As shown in the same section, the maximum relative error between solutions does not change much for this range of resolutions, which indicates that the resolution probably must be increased quite a lot to reach a stable magnitude for solutions. The same changes in the solutions are also observed for the other jet configuration. Despite this, the resolution was usually sufficient to at least capture many features of the differential diffusion profiles to a satisfactory degree.

The turbulent intensity along the jet centerline, is assumed to have points with the highest turbulent intensities of the computational domain. Therefore, this line is suitable for assessing the resolution. For the $\mathrm{Re} = 2000$ jet, the turbulent properties are quite weak and therefore the Kolmogorov scales are quite large as a consequence. Hence, the Kolmogorov scales were resolved 50 - 200 times at the centerline points, which should be more than enough. Compared to Maragkos et al. [3], where the Kolmogorov scale is resolved approximately between 1 and 5 times this is much better resolved. Despite this, some strange behaviour is observed in Figure 4.31, for example the upstream profile exhibiting less differential diffusion than the next downstream profile. However, this may also be explained by the influence of the air co-flow, and is not necessarily an artefact of poor resolution. The weak turbulent behaviour and a jet velocity only double the co-flow velocity, may have caused undiscovered inaccuracies in the UDF calculations, and perhaps the co-flow effect could explain why the differential diffusion was more pronounced for a profile further downstream, which was contrary to most other data.

For $\mathrm{Re} = 4000$ and 8000, the resolution was set to 140, and for the centerline Kolmogorov was resolved between 12 - 140 times, compared to Maragkos' 1-10. Similarly, for the highest Reynolds numbers, resolutions lay between 2 and 39 Kolmogorov scales. Typically, the Kolmogorov scale would be most poorly resolved near the inlet (or potential core) as usual, and the resolution requirements became stricter each time the Reynolds number was increased, as expected. To summarise, all of the jets should be sufficiently resolved for the turbulent flow considered here, but in some cases it could be better in order to also get reliable results for the potential core.

Chapter 6

Conclusion

The thesis addresses the simulation procedure and outcome for hydrogen-rich turbulent jets using LEM3D. Two distinct jet cases were treated; one 90% H_2 and 10% Freon 22 ($CHClF_2$) mixture jet issuing into air, and one 64% CO_2 and 36% H_2 mixture jet in an 1.5 m/s air co-flow. All percentages were taken with respect to mole fractions. ANSYS Geometry, Mesh and Fluent, were used to prepare a steady-state mean velocity field, and turbulent properties for the jets in question. By using user defined functions (UDFs), which were modified versions of UDFs written by SINTEF, the ANSYS results were converted into suitable input for the LEM3D code. The LEM3D code provided by SINTEF was initially written for sequential operation only, but was rewritten to work for parallel computation of LEM 1D domain processes such as molecular diffusion and triplet map events. Some simple tests for parallelisation performance, in terms of a rough refinement exercise and multithreading vs. single threaded cores were performed to find that the parallelisation could potentially greatly reduce run time. Finally, the different simulations were run for both jet mixtures, while varying RANS and LEM resolution, but also Reynolds numbers. The results are a set of radial differential diffusion profiles at different downstream positions in the jet, given as both mean and root-mean-squared values.

The results were compared to different experimental and computational data. Results for the H_2/Freon 22 jet were compared to computational data by Dibble et al. [1], where the computational data was found to underestimate the experimental data by almost an order of magnitude. In addition, the trend with refinement of LEM resolution would cause the underestimation to grow even more. The LEM3D simulations based on the modified RANS mesh was found to match the experimental data best, both in magnitude and by predicting the radial positions for intersections between different downstream z-profiles. The CO_2/H_2 jet results were compared to LES results for mean differential diffusion, where they were found to have vaguely similar behaviour, but also to overestimate the LES results by at most well over an order of magnitude. z_{rms}-values for the jet were plotted together with experimental data by Smith et al. [2], and even though the LEM3D data in some areas had almost oscillatory like behaviour the general trend line would match experiments well, and values would be both over and underestimated but by maximum a factor of 3.

The general trend in the results were that the LEM3D, seems to predict large levels of differential diffusion near the jet center axis, at least upstream near the inlet, and then an almost uniform level throughout the rest of the jet. This behaviour lasts until the edge of the jet at δ_{edge}, but quickly decays to zero outside of this limit.

There are several interesting findings in the results produced for this thesis. One, being that the LEM3D seems to capture the decreasing effects of differential diffusion with higher Reynolds numbers. Another is that by modifying the RANS solution to a coarser resolved mesh, memory requirements can be decreased while still preserving the turbulent properties of the finest resolved solution well. Despite this, the LEM3D solution still appears to be highly dependent upon both LEM resolution and RANS resolution, giving some distinct dissimilarities in the resulting differential diffusion profiles.

For future work it is recommended that the LEM resolution in particular is increased even further, since the level where the differential diffusion magnitude stops falling with resolution is not yet reached. Finer LEM resolutions in conjunction with finer resolved RANS mesh input is also recommended, to get a precise comparison to the LEMres = 512 solution for the fine and modified solutions as well. To this end it would also be very beneficial to make the LEM3D code more affordable in terms of RAM requirements, which tends to grow outside of bounds for personal computers when run in parallel execution. In any case, to fully benefit from the parallelisation, it is necessary to have access to resources on par with Idun, as previously described or even faster, larger computing systems. Most important would however be to correct for the errors discovered in inlet boundary conditions for the finest resolved input, as this would probably make results even more precise.

Bibliography

[1] R. W. Dibble, A. R. Kerstein, M. B. Long, B. Yip, and K. Lyons, “Measurement and computation of differential molecular diffusion in a turbulent jet,” in *Turbulence and Molecular Processes in Combustion*, 1993, pp. 303–310.

[2] L. Smith, R. Dibble, and L. Talbot, “Laser Raman scattering measurements of differential molecular diffusion in nonreacting turbulent jets of H_2/CO_2 mixing with air,” *Physics of Fluids*, vol. 7, no. 6, pp. 1455–1466, 1995.

[3] G. Maragkos, P. Rauwoens, D. Fauconnier, and B. Merci, “Large eddy simulations of differential molecular diffusion in non-reacting turbulent jets of $\mathrm{H}_2/\mathrm{CO}_2$ mixing with air,” *Physics of Fluids*, vol. 26, no. 2, 2014.

[4] K. Mazloomi and C. Gomes, “Hydrogen as an energy carrier: Prospects and challenges,” *Renewable and Sustainable Energy Reviews*, vol. 16, no. 5, pp. 3024–3033, June 2012.

[5] M. Ball and M. Weeda, “The hydrogen economy – Vision or reality?” *International Journal of Hydrogen Energy*, vol. 40, no. 25, pp. 7903–7919, July 2015.

[6] A. Demirbas, “Future hydrogen economy and policy,” *Energy Sources, Part B: Economics, Planning, and Policy*, vol. 12, no. 2, pp. 172–181, 2017.

[7] B. De Colvenaer and C. Castel, “The Fuel Cells and Hydrogen Joint Undertaking (FCH JU) in Europe,” *International Journal of Low-Carbon Technologies*, vol. 7, no. 1, pp. 5–9, March 2012.

[8] P. Sathiah, E. Komen, and D. Roekaerts, “The role of CFD combustion modeling in hydrogen safety management—part I: Validation based on small scale experiments,” *Nuclear Engineering and Design, Supplement C*, vol. 248, pp. 93 – 107, 2012.

[9] A. Kerstein, “Linear-eddy modeling of turbulent transport. Part 3. Mixing and differential molecular-diffusion in round jets,” *Journal of Fluid Mechanics*, vol. 216, pp. 411–435, July 1990.

[10] A. Kerstein, "Linear-eddy modelling of turbulent transport. Part 7. Finite-rate chemistry and multi-stream mixing," *Journal of Fluid Mechanics*, vol. 240, pp. 289–313, 1992.

[11] S. Sannan, T. Weydahl, and A. Kerstein, "Stochastic simulation of scalar mixing capturing unsteadiness and small-scale structure based on mean-flow properties," *Flow, Turbulence and Combustion*, vol. 90, no. 1, pp. 189–216, 2013.

[12] A. Validi and F. Jaberi, "Numerical Study of Turbulent Jet Ignition in a Lean Premixed Configuration," *Flow, Turbulence and Combustion*, vol. 100, no. 1, pp. 197–224, Jan 2018.

[13] M. Dharavath, P. Manna, and D. Chakraborty, "Numerical Simulation of Hydrogen Air Supersonic Coaxial Jet," *Journal of The Institution of Engineers (India): Series C*, vol. 98, no. 5, pp. 575–585, Oct 2017.

[14] T. Weydahl, "A framework for mixing-reaction closure with the Linear Eddy Model," Thesis for the degree of Philosophiae Technology, Norwegian University of Science and Technology, Faculty of Engineering Science and Technology, Department of Energy and Process Engineering, June 2010.

[15] R. Bilger, "Molecular Transport Effects in Turbulent Diffusion Flames at Moderate Reynolds Number," *AIAA journal*, vol. 20, no. 7, pp. 962–970, 1982.

[16] S. Sannan and A. R. Kerstein, "Differential Molecular Diffusion in a Hydrogen-Rich Jet," *Energy Procedia*, vol. 86, pp. 304–314, January 2016.

[17] S. Sannan and A. R. Kerstein, "Numerical Simulation of Differential Molecular Diffusion Effects in a Hydrogen-rich Turbulent Jet Using LEM3D," *Energy Procedia*, vol. 51, pp. 253–258, 2014.

[18] F. M. White, *Viscous fluid flow*, 3rd ed., ser. McGraw-Hill series in mechanical engineering. Boston: McGraw-Hill Higher Education, 2006.

[19] I. S. Ertesvåg, *Turbulent strøyming og forbrenning : Frå turbulensteori til ingeniørverkty*. Trondheim: Tapir akademisk forlag, 2000.

[20] P. McMurtry, "12 Linear Eddy Model of Turbulent Mixing," Lecture notes, March 2001, University of Utah, Salt Lake City, UT, USA. [Online, accessed 17.11.2017]. Available: http://www.eng.utah.edu/~mcmurtry/Turbulence/turbulence.html.

[21] W. H. Kim and T. S. Park, "Effects of Noncircular Inlet on the Flow Structures in Turbulent Jets," *Journal of Applied Mathematics and Physics*, vol. 1, no. 6, pp. 37 – 42, 2013.

[22] P. A. McMurtry, S. Menon, and A. R. Kerstein, "Linear eddy modeling of turbulent combustion," *Energy Fuels*, vol. 7, no. 6, pp. 817–826, Nov. 1993.

[23] ANSYS Inc., "ANSYS - home page," [Online, visited 08.06.18], Available: https://www.ansys.com/, 2018.

[24] W. Massman, “A review of the molecular diffusivities of H_2O, CO_2, CH_4, CO, O_3, SO_2, NH_3, N_2O, NO, and NO_2 in air, O_2 and N_2 near STP,” *Atmospheric Environment*, vol. 32, no. 6, pp. 1111 – 1127, 1998.

Appendices

Appendix A: Literature Search

During the thesis work, information and data had to be retrieved from external sources. The most important tool in this context has been the university library service NTNU UB's Oria system. Among its resources the SCOPUS, Reaxys, INSPEC and Web of Science (ISI) databases have been predominantly used. The Reaxys database have been used for looking up and confirming values of physical properties rather than finding literature sources. The first two databases are operated by commercial Elsevier Business and INSPEC is run by the Institution of Engineers and Technology (IET). Therefore, is natural to suspect that the search result found in these databases may be somewhat biased according to the policies of these organisations. The Web of Science is run by Clarivate Analytics, which claims that the database is without bias, and is generally recognised among my peers and superiors to be a trusted source of information.

When using for example SCOPUS, I have actively used operator commands to limit or widen the search to the most relevant results, see Table A.1 for an example of a search procedure. In this example, I was able to limit a search returning over 7700 results to less than 30, making it easier to find sources that were of interest. The search could be narrowed down even further if necessary. In this specific example the truncation, *, OR- and AND-operators were used. The truncation operator, *, allows any word that is an extension of the word the operator is applied on to be a search result. It can also be used at the front of the word, allowing any word ending with the tagged root word to be a result.

Search sequence	**Search query**	**# of results**
1	hydrogen AND jet	7785
2	hydrogen AND turbulent AND jet	955
3	(H2 OR hydrogen) AND turbulent AND jet	1029
4	(H2 OR hydrogen) AND turbulent AND jet AND (computat* OR numeric*)	470
5	(H2 OR hydrogen) AND turbulent AND jet AND (computation* OR numeric*) AND “Differential Diffusion”	27

Table A.1: A sequence of search queries entered in SCOPUS, and the number of returned result of each query.

This was a short demonstration on how relevant information was collected, but is not of technical interest for the contents of the thesis.

Appendix B: Parameter Configurations

Tables B.1 and B.2, show the configuration for which the final simulations were performed for the $H_2/\text{Freon } 22$ and H_2/CO_2 jets respectively. The parameters in Table B.3, were used for all final simulations producing the differential diffusion data presented the results section. Two exceptions applies to the $\text{Re} = 32000$ and $\text{Re} = 4000$ CO_2/H_2 jets, as rstmod was set to 2500, and 4000 respectively.

RANS resolution	**LEMres**	**lkfac**	**RANSdx**	**DfM(1)**	**DfM(2)**	**Re**
$23 \times 23 \times 38$	128	8	0.4697	0.77	0.12	20000
$23 \times 23 \times 38$	256	4	0.4697	0.77	0.12	20000
$23 \times 23 \times 38$	512	2	0.4697	0.77	0.12	20000
$69 \times 69 \times 114$	42	8	0.1566	0.77	0.12	20000
$69 \times 69 \times 114$	84	4	0.1566	0.77	0.12	20000
$23 \times 23 \times 38*$	128	8	0.4697	0.77	0.12	20000
$23 \times 23 \times 38*$	256	4	0.4697	0.77	0.12	20000

Table B.1: Table showing the most important input parameters used when running the simulations yielding the presented results. This table treats the H_2/Freon 22 jet. Molecular diffusivity, DfM, values are given in units cm^2 s^{-1}, while RANSdx is given in cm. * denotes that RANS data has been modified to this resolution from an originally finer mesh.

RANS resolution	**LEMres**	**lkfac**	**RANSdx**	**DfM(1)**	**DfM(2)**	**Re**
$23 \times 23 \times 70$	90	8	0.6824	0.77	0.14	2000
$23 \times 23 \times 70$	140	8	0.6824	0.77	0.14	4000
$23 \times 23 \times 70$	140	8	0.6824	0.77	0.14	8000
$33 \times 33 \times 70$	100	8	0.6824	0.77	0.14	16000
$41 \times 41 \times 70$	100	8	0.6824	0.77	0.14	32000
$33 \times 33 \times 70$	100	8	0.6824	0.77	0.14	64000

Table B.2: Table showing the most important input parameters used when running the simulations yielding the presented results. This table treats the CO_2/H2 jet. Molecular diffusivity, DfM, values are given in units cm^2 s^{-1}, while RANSdx is given in cm.

Parameter	**Value**
Nt	50000
datcst	20000
datmod	50
varmod	100
velmod	1000
CFL	0.1
PrT	0.7
rotfac	1.0
isrc	0
srcloc	0
comp	0
rstmod	5000

Table B.3: The parameters used for all simulations yielding the presented results.

Appendix C: MatLab Code

Here, a piece of code written to interpolate between and plot differential diffusion profiles produced by the LEM3D code is presented.

```
% Script reading output rms differential diffusion data and
% calculating the interpolation between two positions,
% before plotting of the root-mean-squared radial profiles.
% Written by Nikolai Lid Bjoerdalsbakke, May 2018
clear all
close all
clc

%%Initialization
% Load data
data = load('sim_zrmslemr_transverse_512Coarse.dat');
[m,n] = size(data);

magnfac = 1000;

% Set x-axis positions in numbers of jet radii
pos1 = 10;
pos2 = 20;
pos3 = 30;

Dj = 0.53;
dxRANS = 0.4697;

% Compute distance to the first given profile
% given in number of 3DCV indices
distparam1= pos1*Dj/dxRANS + 0.5;
distparam2= pos2*Dj/dxRANS + 0.5;
distparam3= pos3*Dj/dxRANS + 0.5;

while (distparam1 > 1.0)
    distparam1 = distparam1 -1.0;
end
while (distparam2 > 1.0)
    distparam2 = distparam2 -1.0;
end
while (distparam3 > 1.0)
    distparam3 = distparam3 -1.0;
end

% Calculating slopes of linear interpolations
```

```
a1 = (data(:,3)-data(:,2))/dxRANS;
a2 = (data(:,5)-data(:,4))/dxRANS;
a3 = (data(:,7)-data(:,6))/dxRANS;

% Calculating new profiles at distances found by distparams
prof1 = data(:,2)+a1*distparam1*dxRANS;
prof2 = data(:,4)+a2*distparam2*dxRANS;
prof3 = data(:,6)+a3*distparam3*dxRANS;

%% x = 10 Dj plot
figure(1)
plot(data(:,1)/Dj,prof1*magnfac)
xlabel('r/D_j')
ylabel('10^3 \times z_{rms}')
title('Differential diffusion in radial direction at x = 10 D_j')
axis([0 4 0 55])

%% x = 20 Dj plot
figure(2)
plot(data(:,1)/Dj,prof2*magnfac)
xlabel('\it{r/D_j}')
ylabel('10^3 \times z_{rms}')
title('Differential diffusion in radial direction at x = 20 D_j')
axis([0 4 0 40])

%% x = 30 Dj plot
figure(3)
plot(data(:,1)/Dj,prof3*magnfac)
xlabel('\it{r/D_j}')
ylabel('10^3 \times z_{rms}')
title('Differential diffusion in radial direction at x = 30 D_j')
axis([0 4 0 40])

%% Collectionplot
figure(4)
plot(data(:,1)/Dj,prof1*magnfac,'b-',data(:,1)/Dj,...
    prof2*magnfac,'r-',data(:,1)/Dj,prof3*magnfac,...
    'k-')
xlabel('\it{r/D_j}')
ylabel('10^3 \times \it{z_{rms}}')
title('Differential diffusion in radial direction at various center axis positions',...
```

```
    'FontSize',12)
axis([0 10 -10 30])
legend('\it{x/D_j = 10}','\it{x/D_j = 20}','\it{x/D_j = 30}')

%% Plots for the measurements by Dibble et al.

data1 = load('Kerstein_xd10.txt');
data2 = load('Kerstein_xd20.txt');
data3 = load('Kerstein_xd30.txt');

figure(5)
plot(data(:,1)/Dj,prof1*magnfac,'b-',data(:,1)/Dj,...
    prof2*magnfac,'r-',data(:,1)/Dj,prof3*magnfac,...
    'k-')
hold on
plot(data1(:,1)/Dj,data1(:,2),'b--')
plot(data2(:,1)/Dj,data2(:,2),'r--')
plot(data3(:,1)/Dj,data3(:,2),'k--')
title('Comparison to measured differential diffusion','FontSize',12)
xlabel('\it{r/D_j}')
ylabel('\it{z_{rms}}')
axis([0 10 0 45])
legend('LEM3D, \it{x/D_j = 10}',...
    'LEM3D, \it{x/D_j = 20}',...
    'LEM3D, \it{x/D_j = 30}',...
    'Exp., \it{x/D_j = 10}',...
    'Exp., \it{x/D_j = 20}',...
    'Exp., \it{x/D_j = 30}')
```